Blast-loading simulators: Multiscale design of graded cellular projectiles considering projectile–beam coupling effect

Yuanrui Zhang [a], Yudong Zhu [a], Baixue Chang [a], Jilin Yu [a], Zhijun Zheng [a,b,*]

[a] CAS Key Laboratory of Mechanical Behavior and Design of Materials, Department of Modern Mechanics, University of Science and Technology of China, Hefei, 230027, China
[b] State Key Laboratory of Nonlinear Mechanics, Institute of Mechanics, Chinese Academy of Science, 15 Beisihuan West Road, Beijing, 100190, China

ARTICLE INFO

ABSTRACT

Graded cellular materials with a proper design may simulate blast loading and can be applied to test the anti-blast performance of protective structures. A multiscale design strategy is proposed to obtain the density distribution and mesostructure of graded cellular projectiles when taking a clamped beam as a protective structure and an exponential attenuation load as the simulation target. A projectile–target coupling model is developed for determining the projectile density distribution, and the dimensionless governing equations containing two kinds of dimensionless parameters, namely target-independent parameters and coupling parameters, are obtained. The closed-cell mesostructure of a graded cellular projectile is generated through the Voronoi technique, and the cell configuration parameters are optimized to achieve the designed density distribution while ensuring manufacturability. The graded cellular projectiles are prepared by using 3D printing technology, and their load simulation effects are verified through numerical simulations and impact tests. Case studies demonstrate the necessity of considering the projectile–target coupling effect in the density design. The applicable test condition and selection method of initial parameters of graded cellular projectiles are analyzed with dimensionless parameters. It is found that the initial momentum of the projectile mainly governs its effective simulation duration. With the increase of the initial momentum, the effective simulation duration increases, and the initial momentum should be less than the total impulse of the simulated blast load. The impact technique of well-designed graded cellular projectiles shows great potential in simulating various blast loadings and testing novel protective structures in a laboratory environment.

1. Introduction

An explosion is an extremely destructive situation, which may occur in military confrontation, industrial, and even civil environments (Ngo et al., 2007). A large number of protective structures have been designed and developed to improve the survivability of structures and occupants (Schenk et al., 2014; Wang et al., 2009, 2018a; Yang et al., 2020). Numerical simulation methods of blast loading have been developed extensively (Børvik et al., 2011; Wei et al., 2013; Wadley et al., 2013), but experimental studies on the anti-blast properties of protective structures are limited due to the danger, complexity, and strict requirements of field trials (Gan et al., 2020). Developing laboratory-scale test methods that can simulate blast loading is beneficial

to carry out the performance test and optimal design of protective structures (Aune et al., 2016). However, the blast loading produced by the explosion is strong with complicated characteristics of instantaneity, high intensity, and nonlinear attenuation (e.g., exponential attenuation). Thus, realizing an accurate simulation of blast loading in the laboratory environment is a great challenge.

Some experimental techniques that attempt to simulate blast loading were developed in the laboratory environment. For example, a specially designed flyer plate impact experiment was designed and implemented in a water chamber to generate an impulsive load (Espinosa et al., 2006), an experimental device combining a specifical elastomer and a hydraulically driven piston was constructed to achieve the blast-like loading on structures (Rodriguez-Nikl et al., 2011; Freidenberg et al., 2014), and a wedge-shaped shock tube was constructed to reproduce the free-field blast (Gan et al., 2021, 2020). Compared with the above blast-loading simulators, a simpler and more controllable testing method by launching a metal foam projectile was proposed to generate the shock loading on protective structures (Radford et al., 2005). However, the rectangular-like pressure pulse produced by uniform foam projectiles significantly differs from the exponentially attenuating blast load. Even so, uniform cellular projectiles have been widely applied to investigate the dynamic mechanical performance of various protective structures due to their convenience and controllability (Radford et al., 2006b; Rathbun et al., 2006; Jing et al., 2011; Wang et al., 2011a; Xiao et al., 2019; Wang et al., 2020).

Introducing density gradient into the cellular projectile may solve the difficulties of achieving a blast-like load. Due to the layer-by-layer deformation mode of cellular material under dynamic impact (Zheng et al., 2014; Sun and Li, 2018), the crushing stress can be regulated by density design based on the plastic shock wave theory (Wang et al., 2013b). Thus, graded cellular materials have outstanding designable mechanical properties (Wang et al., 2011b; Shen et al., 2013; Liu et al., 2015). Some researchers have shown that the use of graded cellular material can achieve the required crashworthiness design, e.g., maintaining a constant impact force (Yang et al., 2017; Chang et al., 2020, 2023), which can be applied in anti-collision and other fields. Inspired by the crashworthiness design, choosing a proper density gradient for a cellular projectile may make it possible to simulate blast loading. A linear density-graded metal foam material was applied in the loading simulation (Li et al., 2019), and the triangular pressure pulse formed by it still has a certain deviation from the blast load. This implies that a graded cellular projectile without reasonable design is still difficult to achieve the blast loading with a specific attenuation form. In addition, in the previous design of cellular projectiles, the impacted target was regarded as rigid to simplify the theoretical analysis, while the actual targets were flexible and deformed under the impact of cellular projectiles. The rationality of this idealized test situation and its influence on the projectile design need to be explored.

In a real explosion, the impacted target moves or deforms due to the interaction between the fluid, such as air and water, and the target. The resulting rarefaction wave causes pressure attenuation, making the pressure on the flexible target lower than that on a clamped rigid target (Fleck and Deshpande, 2004). Similarly, due to the coupling relation of force, displacement, and velocity between the projectile and target, the target deformation also affects the impact process of projectiles. However, the impact of cellular projectiles was often regarded as an impulse loading rather than a force loading and isolated from the response process of targets (Qiu et al., 2005). This equivalent method has been proved to be inappropriate through theory and experiments (Radford et al., 2006a), while the projectile–target coupling mechanism and the actual load acting on the deformable targets are still unclear. Recently, a coupling analysis model was proposed by Zhang et al. (2022) to describe the dynamic response process of a uniform cellular projectile impacting a deformable target. The coupling analysis model can accurately predict the actual impact pressure generated by the uniform cellular projectile on the deformable target, which is inconsistent with the load when impacting the rigid target and also different from the blast load. Therefore, the projectile–target coupling effect should be involved in the design of graded cellular projectiles, and a creditable theoretical design model for density gradient is urgent to be developed.

Usually, it is difficult to precisely prepare a pre-designed graded cellular material, and thus the practical application of graded cellular materials is limited. Traditional preparation processes (Banhart, 2001), such as direct foaming (Huang et al., 2019), powder compact melting (Duarte and Banhart, 2000), and investment casting (Fischer et al., 2013), cannot meet the demand for preparing graded cellular materials. In recent years, aluminum foams with approximately linear density distribution were fabricated by improving the direct foaming method (He et al., 2014, 2020). However, this technology has some difficulties in handling the repeatable preparation of graded cellular materials with nonlinear gradients. Fortunately, 3D printing technology makes it possible to prepare a graded cellular material for its ability to fabricate pre-designed cellular structures with high repeatability. For example, lattice structures and open-cell metal foams were fabricated by selective laser sintering (EBM) (Murr et al., 2010; Xiao et al., 2017), and plastics-based cellular materials were prepared by fused deposition modeling (FDM) (Chang et al., 2023). Thus, the design, preparation, and application of graded cellular projectiles become feasible by designing the density gradient and mesostructure and employing 3D printing technology.

This study aims to develop a graded cellular projectile that can simulate blast loading acting on a deformable structure and realize its practical application. In Section 2, a multiscale design strategy of graded cellular projectiles, including the theoretical design model of density distribution and the mesostructure design method, is proposed. In Section 3, the finite element simulation and experiment procedures of graded cellular projectiles impacting flexible targets, including additive preparation, test setup, and data processing methods, are performed. In Section 4, the impact response of graded cellular projectiles, including deformation mode, velocity variation, and impact pressure, is presented. In Section 5, cases of different cellular projectiles impacting different targets are compared, and the applicable test conditions and parameter selection method of graded cellular projectiles are analyzed. Conclusions are presented in Section 6.
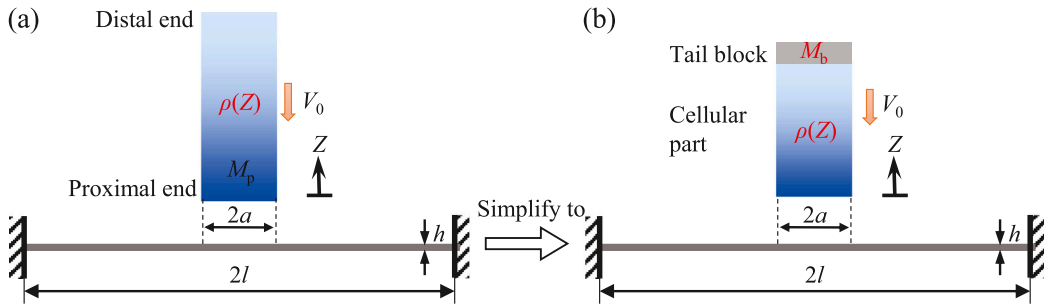
Fig. 1. Schematic diagram of a graded cellular projectile impacting a clamped beam: (a) an initial design, and (b) a simplified design.

2. Multiscale design method

2.1. Problem description

We consider a graded cellular projectile with a mass of M_p, an initial velocity of V_0, and a section dimension of $2a$ impinging a clamped flexible beam, as shown in Fig. 1(a). In principle, the relative density distribution $\rho(Z)$ of the graded cellular projectile to be designed should decrease monotonically to simulate the blast-like impact loading with dramatic attenuation. However, non-monotonic changes may be needed in the density distribution when considering the target deformation in the design. The anti-blast properties of common protective structures, such as monolithic beams and sandwich beams, have attracted much attention (Fleck and Deshpande, 2004; Qiu et al., 2005; Ngo et al., 2007; Latourte et al., 2011). For representativeness and simplicity, a clamped monolithic beam is regarded as the impacted target in this study. The analysis model of a sandwich structure under blast loading can be generalized from that of a monolithic beam. The thickness and span of the monolithic beam are h and $2l$, respectively. The width of the projectile in the Y-axial direction (perpendicular to the paper in Fig. 1(a)) is identical to that of the beam, therefore the three-dimensional model can be equivalent to a two-dimensional model. The structures tested by the graded cellular projectile are assumed to have large deflection since most protective structures are greatly deformed during the anti-blast process and their mechanical response is plastic-dominated. Thus, the material of the beam is regarded as rigid–perfectly plastic material with a density of ρ_{beam} and a yield stress of σ_Y. During impact, the pressure, velocity, and displacement at the proximal end of the projectile remain equal to those of the mid-span of the beam. The deformation of the flexible target diminishes the impact pressure due to the projectile–target coupling effect (Fleck and Deshpande, 2004). Thus, the projectile–target coupling effect should be involved in the design of graded cellular projectiles to avoid the deviation of the load simulation effect.

Consider such a blast load that the pressure rises to the peak value p_0 instantaneously and then decays at an exponential rate with a characteristic time constant τ, expressed as (Nian et al., 2012; Aleyaasin et al., 2015; Chen et al., 2016)

$$p(t) = p_0 e^{-t/\tau}, \quad t \geq 0, \tag{1}$$

where t is the time. The blast load $p(t)$ is to be simulated by a graded cellular projectile, i.e., the relative density distribution $\rho(Z)$ of the graded cellular projectile should be designed to make it produce an impact pressure equal to the blast load $p(t)$ on the front face of the beam. Similarly, the present study is applicable to simulate the loads with other different attenuation forms.

Due to the inertia effect, the velocity and the energy of the uncrushed part of the cellular projectile decrease along the Z-axis, and thus the cellular material at the distal free end of the projectile will never be crushed by itself (Wang et al., 2013a). Therefore, when the graded cellular projectile crushing stops, a part of the uncrushed cellular structure still exists in the tail end of the projectile. After that, the crushed and uncrushed parts of the projectile move together. Hence, the uncrushed part of the graded cellular projectile can be replaced by a solid block with an identical mass M_b to simplify the design and manufacture, as shown in Fig. 1(b). A preliminary configuration design is that a graded cellular projectile consists of two parts: one is the cellular part and the other is a tail block attached to the cellular part. It should be emphasized that the premise of adopting this simplified design is that the distal density of the projectile should not be excessively small, otherwise the reflected wave at the interface between the cellular part and the tail block may cause premature local collapse of the distal cellular material, which may lead to the fluctuation of the impact load.

2.2. Density gradient design

2.2.1. A shock wave model of graded cellular projectile

During impact, the proximal end of a cellular projectile is crushed first, and deformation bands are formed and propagate like a shock wave. The shock front separates the compacted portion from the uncompacted one, as shown in Fig. 2(a). Unlike previous studies (Liu et al., 2015; Li et al., 2019), the portion behind the shock front has a velocity since the impact target is deformable in this study. It is assumed that only one shock front propagates from the proximal end to the distal end during impact. The shock wave model based on the single wave hypothesis can well describe the dynamic crushing behavior of cellular materials and has been widely used (Radford et al., 2005; Zheng et al., 2012, 2014; Wang et al., 2013b). It should be noted that the proximal end
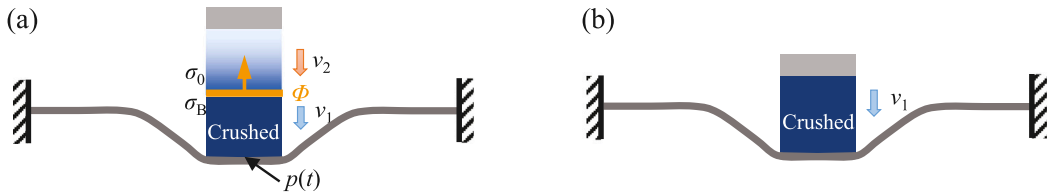
Fig. 2. The impact process: (a) crushing of the projectile, and (b) the end of crushing of the projectile.

of the graded cellular projectile is slightly uneven due to the deformation of the beam, which is ignored in this study for its slight influence. The deformation of the projectile is considered to be one-dimensional, and the loading of the projectile beam is regarded as uniform loading in a mid-span width of $2a$.

The stress–strain (σ–ε) relation of cellular materials with different relative densities under uniaxial compression can be well described by the rigid–plastic hardening (R–PH) idealization proposed by Zheng et al. (2014), written as

$$\sigma = \sigma_0(\rho) + \frac{C(\rho)\varepsilon}{(1-\varepsilon)^2}, \tag{2}$$

where the initial crushing stress σ_0 and the strain hardening parameter C are related to the relative density ρ with a power law

$$\begin{cases} \sigma_0(\rho) = k_1 \sigma_{ys} \rho^{n_1} \\ C(\rho) = k_2 \sigma_{ys} \rho^{n_2} \end{cases}, \tag{3}$$

where σ_{ys} is the yield stress of the cell-wall material, and k_1, n_1, k_2, and n_2 are fitting parameters.

Based on the idealization of cellular materials, the one-dimensional shock wave model of the graded cellular projectile can be constructed. The Lagrangian coordinate system of the graded cellular projectile is established with the proximal end as the coordinate origin. The position of the shock front in this coordinate is Φ, and the shock-front speed is $\dot{\Phi}$. The velocity, stress, and strain ahead of and behind the shock front are $\{v_2(t), \sigma_0(t), 0\}$ and $\{v_1(t), \sigma_B(t), \varepsilon(t)\}$, respectively. According to the one-dimensional shock wave theory (Wang, 2011), the conservation conditions of mass and momentum across the shock front are given as

$$v_1(t) - v_2(t) = -\dot{\Phi}(t)(\varepsilon(t) - 0) \tag{4}$$

and

$$\sigma_B(t) - \sigma_0(\rho) = -\rho_s \rho \dot{\Phi}(t)\left(v_1(t) - v_2(t)\right), \tag{5}$$

respectively, where ρ_s is the density of the base material of the graded cellular projectile. By combining Eqs. (4) and (5), the stress behind the shock front $\sigma_B(t)$ can be obtained as

$$\sigma_B(t) = \sigma_0(\rho) + \frac{\rho_s \rho \left(v_2(t) - v_1(t)\right)^2}{\varepsilon(t)}. \tag{6}$$

From the R–PH idealization of cellular material in Eq. (2), the stress behind the shock front can also be described as

$$\sigma_B(t) = \sigma_0(\rho) + \frac{C(\rho)\varepsilon(t)}{(1-\varepsilon(t))^2}. \tag{7}$$

By combining Eqs. (6) and (7), the strain behind the shock front $\varepsilon(t)$ can be expressed as

$$\varepsilon(t) = \frac{v_2(t) - v_1(t)}{v_2(t) - v_1(t) + c(\rho)}. \tag{8}$$

where $c = \sqrt{C/(\rho\rho_s)}$. By substituting Eq. (8) into Eq. (4), the relation between the shock front speed Φ and the impact velocities v_1 and v_2 is derived as

$$\dot{\Phi}(t) = v_2(t) - v_1(t) + c(\rho), \tag{9}$$

By substituting Eq. (9) into Eq. (5), the stress behind the shock front is rewritten as

$$\sigma_B(t) = \sigma_0(\rho) + \rho_s \rho \left(v_2(t) - v_1(t)\right)\left(v_2(t) - v_1(t) + c(\rho)\right). \tag{10}$$

Since the proximal end of the projectile is subjected to the pressure $p(t)$, the acceleration of the deformed portion behind the shock front is given by

$$\dot{v}_1(t) = \frac{\sigma_B(t) - p(t)}{m_1(t)}, \tag{11}$$

where $m_1(t)$ is the mass per unit area of the deformed portion of the graded cellular projectile. According to the mass conservation, the compressed mass m_1 is identical to the mass of the uncompacted projectile from the proximal end to the shock front position in

the Lagrangian coordinate system, which can be obtained as

$$m_1(t) = \int_0^{\Phi(t)} \rho_s \rho(Z) \mathrm{d}Z. \tag{12}$$

By combining Eqs. (10) and (11), the relation between the impact pressure and the motion of the projectile is obtained as

$$\sigma_0(\rho) + \rho_s \rho \left(v_2(t) - v_1(t)\right) \left(v_2(t) - v_1(t) + c(\rho)\right) - m_1(t)\dot{v}_1(t) = p(t), \tag{13}$$

which indicates that the impact pressure $p(t)$ is regulated by the acceleration $\dot{v}_1$, the velocity difference of v_1 and v_2, and the relative density ρ. The acceleration of the deformed portion ahead of the shock front is determined by

$$\dot{v}_2(t) = \frac{-\sigma_0(\rho)}{m_\mathrm{p} - m_1(t)}, \tag{14}$$

where m_p is the mass per unit area of the graded cellular projectile. Combining Eqs. (13), (9), (12) and (14), we obtain the governing equations describing the motion and shock wave propagation of the graded cellular projectile.

With the velocity v_1 of the deformed portion increasing and the velocity v_2 of the undeformed one decreasing, v_1 and v_2 become equal at a certain time t_e. At this time, the shock front stops moving and the graded cellular projectile stops crushing, as illustrated in Fig. 2(b). After that, the whole projectile moves forward at the velocity of v_1, and the impact load p_1 produced by the projectile cannot be regulated by density design for the disappearance of the shock wave. Therefore, the time t_e is defined as the effective simulation duration of the graded cellular projectile. The total mass per unit area of the crushed cellular material m_c is determined as

$$m_\mathrm{c} = \int_0^{\Phi(t_\mathrm{e})} \rho_s \rho(Z) \mathrm{d}Z, \tag{15}$$

and thus the mass per unit area of the tail block m_b can be given by

$$m_\mathrm{b} = m_\mathrm{p} - m_\mathrm{c}. \tag{16}$$

By substituting the initial conditions of the graded cellular projectile $p(0) = p_0$, $\rho(\Phi(0)) = \rho_0$, $v_1(0) = 0$, $v_2(0) = V_0$, and $\Phi(0) = 0$ into Eq. (13), we have

$$\sigma_{\mathrm{i}0} + \rho_s \rho_0 V_0 \left(V_0 + c(\rho_0)\right) = p_0, \tag{17}$$

where ρ_0 is the relative density of the cellular material at the proximal end of the projectile, and $\sigma_{\mathrm{i}0} = k_1 \sigma_{\mathrm{ys}} \rho_0^{n_1}$ is the initial crushing stress at the proximal end of the projectile. Since the density of matrix material ρ_s, the initial velocity V_0 and the peak value of blast load p_0 are given, and both $\sigma_{\mathrm{i}0}$ and c are functions of ρ_0, the unknown density ρ_0 at the proximal end can be determined from Eq. (17).

2.2.2. A plastic hinge model of the clamped beam

Under the impact of the graded cellular projectile, the clamped beam is subjected to an impact loading equal to the blast load $p(t)$ over a central section of length $2a$. The structural response of the clamped beam under large deflection can be described by a plastic hinge model, which has been applied in many studies (Conroy, 1964; Qiu et al., 2005; Jones, 2011). In this study, the impact load $p(t)$ meets all conditions in Conroy (1964), and the beam is considered to have large deflection. The yield locus of the beam is approximated as a square type, i.e., the bending moment M and axial force N of the beam satisfy (Jones, 2011)

$$|M| = M_0, |N| = N_0, \tag{18}$$

where $M_0 = \sigma_\mathrm{Y} h^2/4$ and $N_0 = \sigma_\mathrm{Y} h$ are the plastic values of the bending moment and longitudinal force, respectively. It is worth mentioning that the accurate yield locus of a monolithic beam or a sandwich beam has been applied to predict the impact response (Qin and Wang, 2009; Qin et al., 2009) by using the membrane factor method (Yu and Stronge, 1990), and the theoretical predictions are more accurate than those obtained by using a square yield locus (Qiu et al., 2003, 2005). However, applying the accurate yield locus of the beam to the design framework may make the governing equation much more complicated. Thus, for simplicity, the square yield locus is adopted in this study. In the impact process of the graded cellular projectile, the monolithic beam begins to deform from the mid-span area (only the right-half beam is analyzed, considering the symmetry of the studied problem). The velocity field $\dot{w}(x,t)$ and deflection field $w(x,t)$ of the beam are usually divided into three phases (Martin and Symonds, 1966), as illustrated in Fig. 3. In Phase 1, two moving plastic hinges are generated on the half beam, the inner plastic hinge moves to the mid-span, the outer plastic hinge moves to the clamped end, and the velocity field of the beam is a trapezoidal distribution. In Phase 2, the inner plastic hinges of the beam reach the mid-span, and the velocity field of the beam changes into a triangular distribution. In Phase 3, the outer plastic hinges reach the clamped ends, and the beam then deforms with a triangular velocity field until the deformation stops. Considering the two motion states of the projectile and three phases of the clamped beam, the whole impact process can be divided into four stages as follows (Zhang et al., 2022). At Stage I, the projectile begins to crush, and the beam motion is in Phase 1. At Stage II, the projectile crush continues, and the beam motion is in Phase 2. At Stage III, the projectile stops crushing, and the beam motion is still in Phase 2. At Stage IV, the projectile continues to move as a whole, and the beam motion is in Phase 3. This study focuses on Stage I and Stage II when the graded cellular projectile keeps crushing and its density gradient is designable. During impact, the mid-span velocity $\dot{w}_0$ and deflection w_0 of the beam are respectively equal to the velocity v_1 and displacement of the proximal end of the projectile due to their coupling relation.
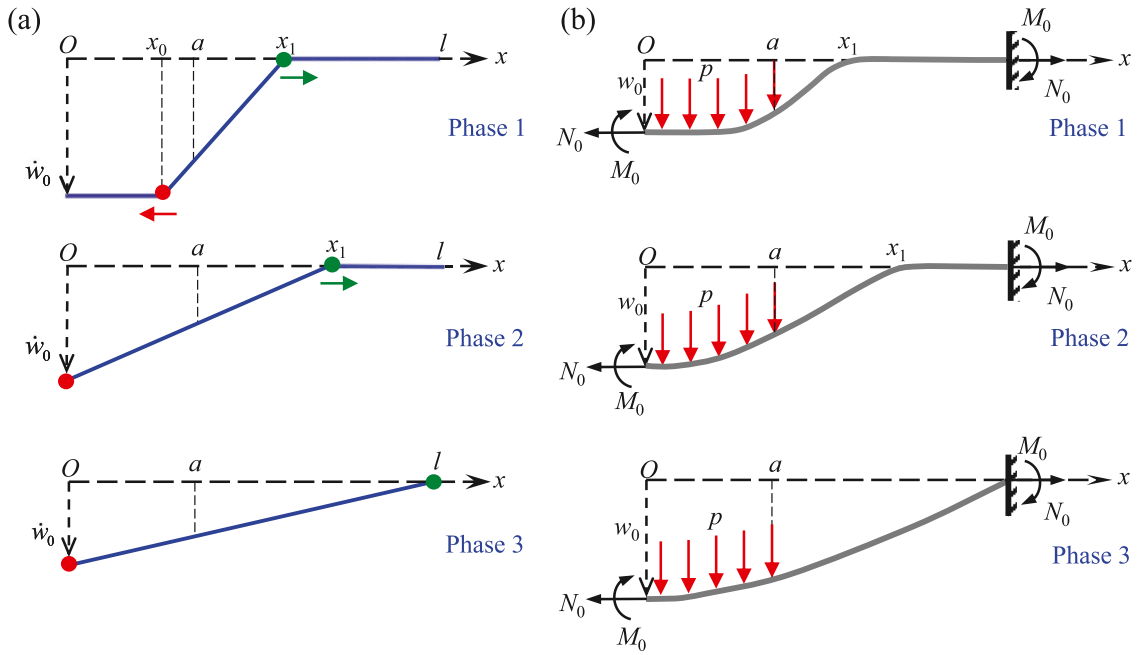
Fig. 3. Schematic diagram of the right-half beam during impact: (a) velocity field and (b) deflection field (Zhang et al., 2022) .

At Stage I, the velocity field of the right-half beam can be expressed as

$$
\dot{w}(x,t) = \begin{cases}
v_1(t), & 0 \leq x \leq x_0(t) \\
\dfrac{x_1(t) - x}{x_1(t) - x_0(t)} v_1(t), & x_0(t) \leq x \leq x_1(t) , \\
0, & x_1(t) \leq x \leq l
\end{cases}
\tag{19}
$$

where x_0 and x_1 are the positions of the inner and outer plastic hinges, respectively. It is worth mentioning that, in the previous studies (Qiu et al., 2005; Qin et al., 2009, 2014), the external loading was usually regarded as the impulse loading, so the central section of the beam was considered to translate at a constant velocity in the initial phase. However, the impact of the graded cellular projectile is force loading, thus the central section of the beam is assumed to translate at a changing velocity $v_1(t)$ in this study. The bending moment changes from M_0 at the inner plastic hinge to $-M_0$ at the outer plastic hinge, and the longitudinal force produced by the tensile deformation is N_0. Since the shear force on the traveling plastic hinge is 0, the resultant force (per unit area of the beam) of the part between the right and left inner plastic hinges is $p(t)$, and the acceleration of this part is (Conroy, 1964)

$$
\dot{v}_1(t) = \frac{p(t)}{m},
\tag{20}
$$

where $m = \rho_{\text{beam}} h$ is the mass per unit area of the beam. Taking the mid-span of the beam as the reference point and using the momentum theorem and the moment of momentum theorem, we have

$$
a \int_0^t p(t) \mathrm{d}t = \int_0^l m \dot{w}(x,t) \mathrm{d}x
\tag{21}
$$

and

$$
2M_0 t + N_0 \int_0^t w_0(t) \mathrm{d}t + \frac{a^2}{2} \int_0^t p(t) \mathrm{d}t = \int_0^l m \dot{w}(x,t) x \mathrm{d}x.
\tag{22}
$$

Compared to the Conroy's work (Conroy, 1964), the momentum moment theorem equation of the beam has a membrane force related term since the large deflection is considered. Substituting the velocity field Eq. (19) into Eqs. (21) and (22) and differentiating the formulas with respect to time t, we obtain

$$
m\dot{v}_1(t) \left(x_1(t) + x_0(t) \right) + m v_1(t) \left(\dot{x}_0(t) + \dot{x}_1(t) \right) = 2a p(t)
\tag{23}
$$

and

$$
\left(2m v_1(t) x_0(t) - B_2 \right) \dot{x}_0(t) + \left(2m v_1(t) x_1(t) - B_2 \right) \dot{x}_1(t) - B_1 \dot{v}_1(t) = 24 M_0 + 12 N_0 w_0(t),
\tag{24}
$$

where B_1 and B_2 are defined as

$$\begin{cases} B_1 = 3ma\left(x_1(t) + x_0(t)\right) - 2m\left(x_0^2(t) + x_0(t)x_1(t) + x_1^2(t)\right) \\ B_2 = 3mv_1(t)a - 2mv_1(t)\left(x_0(t) + x_1(t)\right) \end{cases}. \tag{25}$$

By combining Eqs. (20), (23) and (24), the moving speeds of the inner and outer plastic hinges are given by

$$\dot{x}_0(t) = -\frac{12M_0 + 6N_0w_0(t) + p(t)\left(3a^2 - 2ax_0(t) - 4ax_1(t) + 2x_0(t)x_1(t) + x_1^2(t)\right)}{mv_1(t)\left(x_1(t) - x_0(t)\right)} \tag{26}$$

and

$$\dot{x}_1(t) = \frac{12M_0 + 6N_0w_0(t) + p(t)\left(3a^2 - 4ax_0(t) - 2ax_1(t) + 2x_0(t)x_1(t) + x_0^2(t)\right)}{mv_1(t)\left(x_1(t) - x_0(t)\right)}, \tag{27}$$

respectively. The mid-span velocity is given by

$$\dot{w}_0 = v_1(t). \tag{28}$$

Combining Eqs. (20), (26), (27), and (28), we obtain the governing equations of the beam at Stage I.

At Stage II, as the projectile keeps impacting and crushing, the velocity field of the half beam at Stage II can be expressed as (Qiu et al., 2005; Qin et al., 2009)

$$\dot{w}(x,t) = \begin{cases} \dfrac{x_1(t) - x}{x_1(t)} v_1(t), & 0 \le x \le x_1(t) \\ 0, & x_1(t) \le x \le l \end{cases}. \tag{29}$$

Similarly, substituting Eq. (29) into Eqs. (21) and (22) and differentiating the formulas with respect to time t can obtain

$$mx_1(t)\dot{v}_1(t) + mv_1(t)\dot{x}_1(t) = 2ap(t) \tag{30}$$

and

$$m\dot{v}_1(t)\left(2x_1^2(t) - 3ax_1(t)\right) + m\dot{x}_1(t)\left(4v_1(t)x_1(t) - 3av_1(t)\right) = 24M_0 + 12N_0w_0(t). \tag{31}$$

By combining Eqs. (30) and (31), the mid-span velocity and the moving speed of the outer hinge are obtained as

$$\dot{v}_1(t) = -\frac{12M_0 + 6N_0w_0(t) + p(t)\left(3a^2 - 4ax_1(t)\right)}{mx_1^2(t)} \tag{32}$$

and

$$\dot{x}_1(t) = \frac{12M_0 + 6N_0w_0(t) + p(t)\left(3a^2 - 2ax_1(t)\right)}{mv_1(t)x_1(t)}, \tag{33}$$

respectively. Combining Eqs. (28), (32) and (33), we obtain the governing equations of the beam at Stage II.

Substituting the initial conditions of the beam $p(0) = p_0$, $v_1(0) = 0$, and $w_0(0) = 0$ into the governing equations of the beam, i.e., Eqs. (20), (26), (27) and (28), the initial positions of the inner and outer plastic hinge of the right-half beam are obtained as

$$x_0(0) = a - \sqrt{12M_0/p_0} \tag{34}$$

and

$$x_1(0) = a + \sqrt{12M_0/p_0}, \tag{35}$$

respectively, which are consistent with the initial positions of plastic hinges obtained by Conroy (1964) without considering the longitudinal force N_0. Here, it should be noted that when the initial velocity field is a trapezoid, $x_0(0) > 0$, i.e. $a > \sqrt{12M_0/p_0}$. Therefore, in the case of $a < \sqrt{12M_0/p_0}$, the inner plastic hinges can only be formed on the mid-span of the beam, the initial field is triangular, and the dimensionless density design equations of the projectile change to Eqs. (28), (32) and (33). Meanwhile, the initial position of the outer plastic hinge of the right-half beam is obtained as

$$x_1(0) = \frac{3}{2}a + \frac{6M_0}{ap_0}. \tag{36}$$

It should be noted here that the cell number on the same cross-section of the projectile decreases as the section dimension a decreases, which may lead to a strong fluctuation of the impact load. This issue may be solved by reducing the cell-wall thickness to increase the cell number, but the projectile with excessively small section dimension is not recommended in an impact test considering the limited printing accuracy.

For a specific blast load to be simulated, according to the coupling relationship between the velocity, displacement, and impact pressure of the projectile and the beam, the governing equations of density design of the graded cellular projectile are obtained by combining the governing equations of the projectile, i.e. Eqs. (13), (9), (12) and (14), and the governing equations of the beam, i.e. Eqs. (20), (26), (27) and (28) at Stage I and Eqs. (28), (32) and (33) at Stage II. The density design procedure of the graded
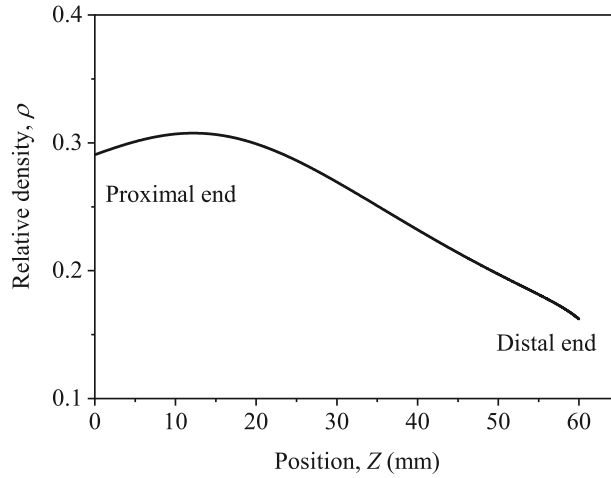
Fig. 4. A design case of the graded cellular projectile to simulate a blast load of $p_0 = 15$ MPa and $\tau = 0.2$ ms, an impacted clamped beam of $\rho_{\mathrm{beam}} = 7750$ kg/m^3, $h = 3$ mm, $\sigma_Y = 400$ MPa, cellular material parameters of $\sigma_{\mathrm{ys}} = 42$ MPa, $k_1 = 1.53$, $n_1 = 2.30$, $k_2 = 0.30$, and $n_2 = 1.89$, and a graded cellular projectile with $m_p = 0.0175$ g/mm^2 and $V_0 = 170$ m/s.

cellular projectile is carried out as follows. By assuming the total mass m_p, initial velocity V_0, and section dimension $2a$ of the graded cellular projectile, with the initial conditions of the projectile and the beam, the density distribution $\rho(Z)$ of the graded cellular projectile can be obtained by solving the governing equations of density design with the Runge–Kutta method, and the mass of the tail block can be calculated from Eqs. (15) and (16). A density design case of the graded cellular projectile is presented in Fig. 4. The density distribution increases first and then decreases from the proximal end to the distal end, showing remarkable nonlinearity and non-monotonicity.

Except for the above-mentioned impact situation that the graded cellular projectile stops crushing in Phase 2 of the beam (which is referred to as Case 2), the projectile may also stop crushing in other phases (Zhang et al., 2022). For example, when the density and the initial velocity of the projectile are large but the total mass is small, the projectile may stop in Phase 1 (referred to as Case 1), i.e., when $v_1(t) = v_2(t)$, $x_0(t) > 0$. For this case, the governing equations of the projectile design are identical to that of Stage I in Case 2. However, Case 1 should be avoided as much as possible in the projectile design since the projectile stops crushing too early, resulting in a short effective simulation duration and poor simulation effect.

When the section dimension a of the projectile is large or the span of the beam is small, the projectile may stop in Phase 3 (referred to as Case 3), i.e., when $x_1(t) = l$, $v_1(t) < v_2(t)$. For Case 3, the impact process while the projectile keeps crushing can be divided into three stages. At Stages I, II and III, the deformation of the beam is in Phases 1, 2 and 3, respectively. The governing equations of Stage I and II in Case 3 are consistent with those of Stages I and II in Case 2. At Stage III of Case 3, the velocity field of the beam can be expressed as (Qiu et al., 2005; Qin et al., 2009)

$$\dot{w}(x,t) = \frac{l-x}{l} v_1(t). \tag{37}$$

The clamped end is taken as the reference point to avoid introducing the shear force on the clamped end, and the moment of momentum theorem equation of the beam can be rewritten as

$$\int_0^t \int_0^a p(\tau)(l-x)\mathrm{d}x\mathrm{d}\tau - 2M_0 t - N_0 \int_0^t w_0(\tau)\mathrm{d}\tau = \int_0^l m\dot{w}(x,t)(l-x)\mathrm{d}x. \tag{38}$$

Substituting Eqs. (37) into Eqs. (38) and differentiating the equation with respect to time t obtains

$$\dot{v}_1(t) = \frac{1}{ml^2}\left[3(l - \frac{1}{2}a)ap(t) - 6M_0 - 3N_0 w_0(t)\right]. \tag{39}$$

By combining the governing equations of the crushing projectile (i.e., Eqs. (13), (9), (12) and (14)) and those of the beam (i.e., Eqs. (28) and (39)), the governing equations of the density design at Stage III can be obtained.

2.2.3. Dimensionless governing equations of density design

We proceed to present the governing equations of density design in dimensionless form. The dimensionless variables of the blast load to be simulated are

$$\bar{p} = \frac{p}{p_0}, \quad \bar{t} = \frac{t}{\tau}, \tag{40}$$

and the dimensionless variables of the graded cellular projectile are

$$\bar{\rho} = \frac{\rho}{\rho_0}, \quad \bar{\sigma}_0 = \frac{\sigma_0}{\sigma_{i0}}, \quad \bar{c} = \frac{c}{\sqrt{\sigma_{i0}/(\rho_s \rho_0)}}, \quad \bar{\Phi} = \frac{\Phi}{m_p/(\rho_s \rho_0)}, \quad \bar{v}_2 = \frac{v_2}{V_0}, \quad \bar{m}_1 = \frac{m_1}{m_p}. \tag{41}$$

In this study, k_1, n_1, k_2, and n_2 are assumed to be known to focus on the influence of the yield stress σ_{ys} of the base material. The dimensionless variables of the clamped beam are

$$\bar{x}_1 = \frac{x_1}{a}, \quad \bar{x}_0 = \frac{x_0}{a}, \quad \bar{w}_0 = \frac{w_0}{h}, \quad \bar{v}_1 = \frac{v_1}{V_0}. \tag{42}$$

Assuming the beam length $2l$ is much longer than the loading area length $2a$ of the projectile, the outer plastic hinge of the beam will keep moving and will not arrive at the clamped end during the graded cellular projectile crushing, which means the design of the projectile is independent of the beam length. Therefore, different from the previous literature (Qiu et al., 2005; Qin et al., 2009), the mid-span deflection w_0 here is dimensionless by the thickness h instead of the length l.

By substituting the dimensionless variables of the projectile, the governing equations of the graded cellular projectile, i.e., Eqs. (13), (9), (12) and (14), are reduced to

$$\begin{cases} \bar{\rho}^{n_1} + \alpha\bar{\rho}\left(\bar{v}_2 - \bar{v}_1\right)\left(\bar{v}_2 - \bar{v}_1 + \sqrt{\frac{k_2}{\alpha k_1}\rho_0^{n_2-n_1}\bar{\rho}^{n_2-1}}\right) = \beta\bar{p} + \beta\gamma\bar{m}_1\frac{d\bar{v}_1}{d\bar{t}} \\ \frac{d\bar{\Phi}}{d\bar{t}} = \frac{\alpha}{\beta\gamma}\left(\bar{v}_2 - \bar{v}_1 + \sqrt{\frac{k_2}{\alpha k_1}\rho_0^{n_2-n_1}\bar{\rho}^{n_2-1}}\right) \\ \frac{d\bar{v}_2}{d\bar{t}} = -\frac{\bar{\rho}^{n_1}}{\beta\gamma\left(1-\bar{m}_1\right)}, \quad \bar{m}_1 = \int_0^{\bar{\Phi}}\bar{\rho}(\bar{Z})\,d\bar{Z} \end{cases}, \tag{43}$$

where the dimensionless parameters are defined as

$$\alpha = \frac{\rho_s\rho_0V_0^2}{\sigma_{i0}}, \quad \beta = \frac{p_0}{\sigma_{i0}}, \quad \gamma = \frac{m_pV_0}{p_0\tau}. \tag{44}$$

Here, α is the ratio of the hydrodynamic pressure to the static initial crushing stress of the cellular material at the proximal end of the projectile, β is the ratio of the blast peak loading to the initial crushing stress at the proximal end, and γ is the ratio of initial momentum of the projectile to the total impulse of the blast loading. Substituting $\sigma_{i0} = k_1\sigma_{ys}\rho_0^{n_1}$ and $c(\rho_0) = k_2\sigma_{ys}\rho_0^{n_2}$ into the initial equation of projectile, i.e., Eq. (17), and simplifying it lead to

$$\sqrt{\frac{k_2}{k_1}\rho_0^{n_2-n_1}} = \frac{\beta - \alpha - 1}{\sqrt{\alpha}}. \tag{45}$$

Substitution of Eq. (45) into Eq. (43) obtains the dimensionless governing equations of the graded cellular projectile

$$\begin{cases} \bar{\rho}^{n_1} + \alpha\bar{\rho}\left(\bar{v}_2 - \bar{v}_1\right)\left(\bar{v}_2 - \bar{v}_1 + \frac{\beta - \alpha - 1}{\alpha}\sqrt{\bar{\rho}^{n_2-1}}\right) = \beta\bar{p} + \beta\gamma\bar{m}_1\frac{d\bar{v}_1}{d\bar{t}} \\ \frac{d\bar{\Phi}}{d\bar{t}} = \frac{\alpha}{\beta\gamma}\left(\bar{v}_2 - \bar{v}_1 + \frac{\beta - \alpha - 1}{\alpha}\sqrt{\bar{\rho}^{n_2-1}}\right) \\ \frac{d\bar{v}_2}{d\bar{t}} = -\frac{\bar{\rho}^{n_1}}{\beta\gamma\left(1-\bar{m}_1\right)}, \quad \bar{m}_1 = \int_0^{\bar{\Phi}}\bar{\rho}(\bar{Z})\,d\bar{Z} \end{cases}. \tag{46}$$

By substituting the dimensionless variables of the beam, the governing equations of the beam at Stage I, i.e., Eqs. (20), (26), (27), and (28), can be rewritten in a dimensionless form as

$$\begin{cases} \frac{d\bar{v}_1}{d\bar{t}} = \frac{\kappa}{\gamma}\bar{p} \\ \frac{d\bar{x}_0}{d\bar{t}} = -\frac{\xi\left[3\eta\left(1+2\bar{w}_0\right) + \bar{p}(3 - 2\bar{x}_0 - 4\bar{x}_1 + 2\bar{x}_0\bar{x}_1 + \bar{x}_1^2)\right]}{\gamma\bar{v}_1\left(\bar{x}_1 - \bar{x}_0\right)} \\ \frac{d\bar{x}_1}{d\bar{t}} = \frac{\xi\left[3\eta\left(1+2\bar{w}_0\right) + \bar{p}(3 - 4\bar{x}_0 - 2\bar{x}_1 + 2\bar{x}_0\bar{x}_1 + \bar{x}_0^2)\right]}{\gamma\bar{v}_1\left(\bar{x}_1 - \bar{x}_0\right)} \\ \frac{d\bar{w}_0}{d\bar{t}} = \zeta\bar{v}_1 \end{cases}, \tag{47}$$

where

$$\xi = \frac{m_p}{\rho_{beam}h}, \quad \eta = \frac{\sigma_Yh^2}{p_0a^2}, \quad \zeta = \frac{V_0\tau}{h}. \tag{48}$$

ξ is the ratio between the mass per unit area of the graded cellular projectile and the mass per unit area of the beam, η represents the moment ratio between the beam and the loading, and ζ is the ratio of the flying distance of the projectile within the time scale of the blast loading to the beam thickness. When $\bar{x}_0(\bar{t}) = 0$, the impact process enters Stage II, the governing equations of the beam

in this stage, i.e., Eqs. (32), (28) and (33), are given in dimensionless form by

$$\begin{cases} \dfrac{d\,\bar{v}_1}{d\,\bar{t}} = -\dfrac{\xi\left[3\eta\left(1+2\bar{w}_0\right)+\bar{p}\left(3-4\bar{x}_1\right)\right]}{\gamma\bar{x}_1^2} \\[2mm] \dfrac{d\,\bar{x}_1}{d\,\bar{t}} = \dfrac{\xi\left[3\eta\left(1+2\bar{w}_0\right)+\bar{p}\left(3-2\bar{x}_1\right)\right]}{\gamma\bar{v}_1\bar{x}_1} \\[2mm] \dfrac{d\,\bar{w}_0}{d\,\bar{t}} = \zeta\bar{v}_1 \end{cases} . \tag{49}$$

When $\eta < 1/3$ with the dimensionless initial conditions $\bar{p}(0) = 1$, $\bar{v}_1(0) = 0$, $\bar{v}_2(0) = 1$, $\bar{w}_0(0) = 0$, $\bar{\rho}(0) = 1$ and $\bar{\Phi}(0) = 0$, the dimensionless initial positions of the inner and outer plastic hinges are obtained through Eq. (47) as

$$\bar{x}_0(0) = 1 - \sqrt{3\eta} \tag{50}$$

and

$$\bar{x}_1(0) = 1 + \sqrt{3\eta}, \tag{51}$$

respectively. When $\eta \geq 1/3$, the dimensionless initial position of the outer plastic hinge of the right-half beam is obtained through Eq. (49) as

$$\bar{x}_1(0) = \frac{3}{2}\left(1+\eta\right). \tag{52}$$

For the simulated blast load (or other attenuation loads), we can solve these dimensionless governing equations to determine the dimensionless density distribution $\bar{\rho}$ of the graded cellular projectile with a numerical method, e.g., the Runge–Kutta method. When the particle velocity behind and ahead of the shock wave is identical, i.e., $\bar{v}_1 = \bar{v}_2$, the numerical calculation is completed, and the dimensionless effective simulation duration $\bar{t}_e$ can be obtained. Thus, we can apply the projectile–target coupling model with a given impact load to obtain an accurate density distribution of the graded cellular projectile. This approach promotes the active design of materials based on mechanical principles.

It can be found that α, β, and γ are extracted from the governing equations of the graded cellular projectile and are only related to the parameters of the projectile and blast load, while ξ, η, and ζ are extracted from the governing equations of the monolithic beam and depend on the parameters of the projectile and blast load as well as the beam. In the case that the mass of the beam is large enough to be approximated as a rigid target, the velocity and acceleration of the mid-span are almost zero, and the density design of the graded cellular projectile is only related to dimensionless parameters α, β and γ and is independent of ξ, η and ζ. When the clamped beam is flexible, that is, the mid-span velocity and acceleration are not zero, the changes of ξ, η, and ζ affect the response of the beam, which further affects the design of graded cellular projectiles. Therefore, ξ, η, and ζ represent the coupling effect between projectiles and targets and the strength of this effect, which are uniformly referred to as "coupling parameters", while α, β, and γ can be called "target-independent parameters". The influence of these two kinds of dimensionless parameters will be discussed later.

2.3. Mesostructure design

Different mesostructure configurations, such as open cell, closed cell, and random honeycomb, are available in constructing graded cellular materials. In this study, the random closed-cell structure is adopted because of its high material utilization and stability of force transmission. The 3D Voronoi technique based on a varying cell-size distribution method has been developed to generate closed-cell structures with a continuous density distribution (Yang et al., 2017; Zheng et al., 2014), which is applied here to construct the mesostructure of the graded cellular projectile with a pre-designed density distribution. The generation process of the cellular structure includes the following steps: seeding cell nuclei in the specified area based on the density design, generating the cellular structure with closed cells, cutting the cellular structure, calculating and verifying the density distribution of the cellular structure, and fine-tuning the cell-wall thickness. The principle of random seeding is that the distance δ_{ij} between any two adjacent nuclei i and j is limited as (Yang et al., 2017; Wang et al., 2011b, 2013b)

$$\delta_{ij} \geq (1-k)\,\delta_{\min}\left(\rho_{ij}\right) = (1-k)\,\frac{3\left(6+\sqrt{3}\right)h_c}{8\rho_{ij}}, \tag{53}$$

where k is the cell irregularity, $\delta_{\min}(\rho)$ is the minimum distance between any two adjacent nuclei i and j in a tetrakaidecahedron structure with relative density ρ, ρ_{ij} is the relative density at the middle point of nuclei i and j, and h_c is the cell-wall thickness.

The configuration design of the graded cellular projectile is carried out by taking the nonlinear density design in Section 2.1 as an example. Here, the tail mass part of the projectile is replaced by a solid block to simplify the modeling and reduce computation. For the cellular part, the regulation mechanism of meso-configuration parameters, i.e., the influence of the cell-wall thickness h_c and the cell irregularity k on the cell configuration and the density distribution, is discussed. Considering that the cell irregularity $k = 0.4$ and three values of the cell-wall thickness h_c, namely $h_c = 0.2$, 0.5, and 0.8 mm, the corresponding cellular configurations and their density distributions are shown in Fig. 5. With the increase of h_c, the cell size of the cellular structure is larger, which is attributed to the decrease of the minimum distance between adjacent nuclei, as presented in Eq. (53). Due to the large cell size
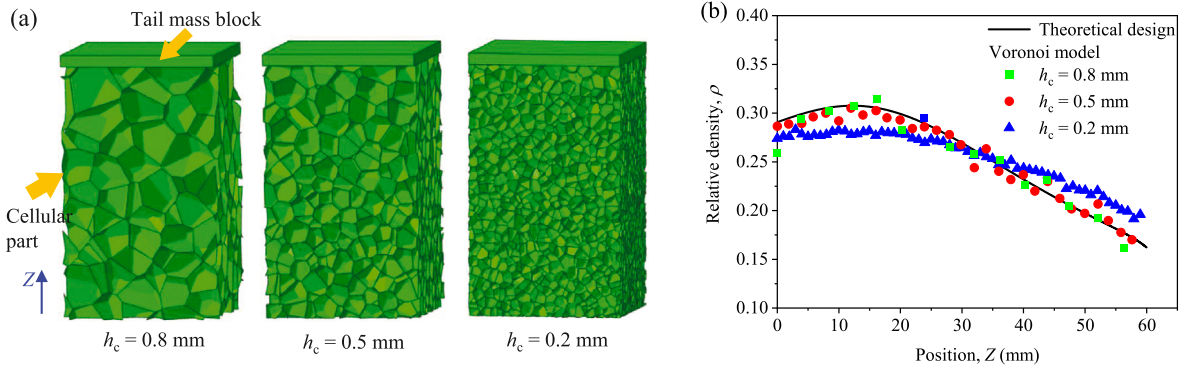
Fig. 5. Graded cellular projectile with different cell-wall thickness h_c: (a) meso-configurations and (b) density distributions.
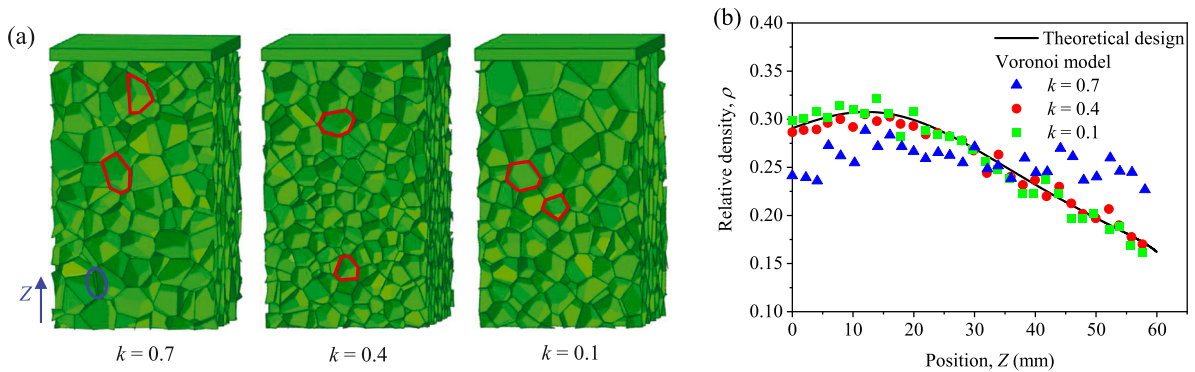

Fig. 6. Graded cellular projectiles with different cell irregularity k: (a) meso-configurations and (b) density distributions.

and a small number of cells, the density of the cellular structure with $h_c = 0.8$ mm oscillates greatly on both sides of the theoretical density curve, and the impact pressure produced by the cellular projectile may show great fluctuation. As h_c decreases and the cell number increases, e.g., $h_c = 0.5$ mm, the density distribution of cellular structure matches well with the pre-designed density. When $h_c = 0.2$ mm, the density distribution with less fluctuation and smoother transition is achieved, but meanwhile the cell size is too small to realize the sharp change of density in a certain distance, showing a great deviation from the pre-designed density. The root mean square errors (RSME) between the density distribution of three projectiles with h_c of 0.2, 0.5, and 0.8 mm and the pre-designed design curve are 0.0199, 0.0077 and 0.0116, respectively. Besides, the realization of thin cell walls requires high precision of 3D printing technology, which increases the difficulty and cost of processing. Extremely small or sharp cells may also appear in the cellular structure with a small cell-wall thickness, leading to poor quality grids in the finite element model and non-convergence or errors in the simulation results. Therefore, excessively small cell-wall thickness should be avoided in the mesostructure design.

Similarly, the cell-wall thickness h_c of 0.5 mm and three values of cell irregularity k of 0.1, 0.4 and 0.7 are considered. For the case of $k = 0.1$, the cell shape is close to the regular polygon. By contrast, for the case of $k = 0.7$, some extremely long and narrow cells are generated, as shown in Fig. 6(a). Cellular structure with small cell irregularity, i.e., too regular cells, may reduce the smoothness of the density distribution curve, while large cell irregularity leads to violent fluctuations in the density distribution, thus unable to capture the trend of the pre-designed density curve. The RSME between the density distribution of three projectiles with k of 0.1, 0.4, and 0.7 and the theoretical design curve is 0.0089, 0.0077, and 0.0399, respectively. As a result, compared with $k = 0.1$ and 0.7, the density distribution of cellular structures with $k = 0.4$ is more consistent with the pre-designed density distribution, as shown in Fig. 6(b). Based on the above analysis, it is important to choose the appropriate meso-configuration parameters to balance the requirements from design, manufacture, and other aspects. In this study, the cell-wall thickness h_c of about 0.5 mm and cell irregularity k of about 0.4 are commended considering the printing accuracy of the 3D printer used.

3. Numerical and experimental methods

3.1. Finite element model

The finite element model of a graded cellular projectile impacting a clamped flexible beam is established by the finite element software ABAQUS/Explicit based on the mesostructure design. In the finite element model, the matrix material of the projectile
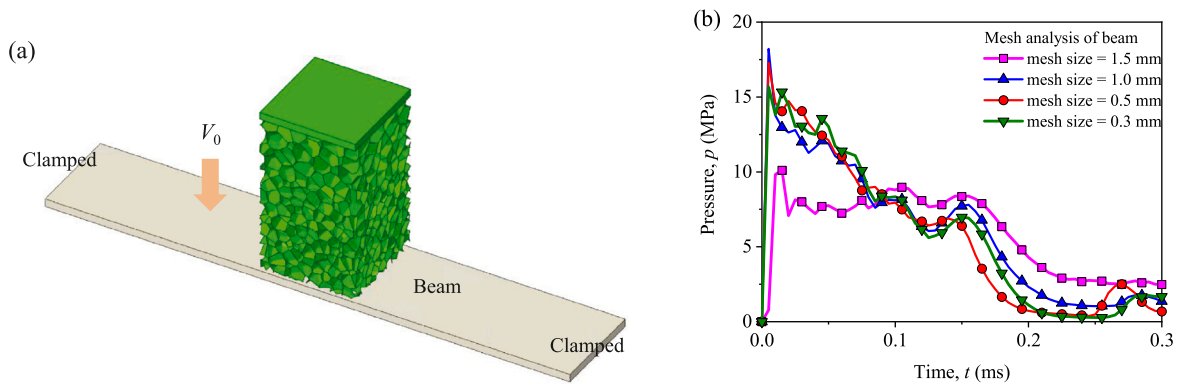
Fig. 7. (a) The finite element model of a cellular projectile impacting a clamped beam and (b) the mesh sensitivity analysis of the finite element model.

and the beam are acrylonitrile butadiene styrene (ABS) plastic and 304 stainless steel, respectively, which are described by the elastic–perfectly plastic material model. Since the dynamic stress enhancement of the cellular material under high-velocity impact is mainly attributed to the inertia effect rather than the strain-rate effect of matrix material (Li et al., 2016), the strain-rate sensitivity of the ABS plastic is not considered in the finite element simulation. Within the range of impact loads considered in this study, the effect of strain-rate sensitivity on the beam response is not significant according to Yang et al. (2018), so the strain-rate effect of the stainless steel is also ignored for simplicity. The density, Young's modulus, Poisson's ratio and yield stress of ABS plastic are set as 966 kg/m^3, 1.6 GPa, 0.3 and 42 MPa, respectively, and those of 304 stainless steel are set as 7689 kg/m^3, 191 GPa, 0.3 and 313 MPa. These material parameters were obtained from experimental tests, which will be detailed in Section 3.2. The cross-section size of the projectile is 36.5 mm × 36.5 mm, i.e., $a = 18.25$ mm. The span and width of the beam are 200 mm × 36.5 mm. The free degrees of the nodes on the left and right end faces of the beam are restricted to realize the fixing constraint on both ends. A *Tie contact is set on the contact surface between the solid block and the cellular structure. All nodes of the projectile have an initial velocity of V_0, as shown in Fig. 7(a). The general contact is adopted, and the friction coefficient is 0.02. Besides, the entrapped air is not considered in the numerical simulation.

The cell walls of the cellular projectile are meshed using hybrid shell elements of type S3R, and the monolithic beam is meshed using the hexahedral solid element of type C3D8R. A mesh sensitivity analysis of finite element models was performed to obtain accurate and stable simulation results. For the graded cellular projectile, the characteristic size of shell elements was set as 0.3 mm according to the mesh sensitivity analysis of the Voronoi cellular material in the literature (Chang et al., 2020; Yang et al., 2017; Zheng et al., 2014). For the monolithic beam, impact numerical tests were performed with different element sizes of 1.5, 1.0, 0.5 and 0.3 mm. Apparently, there are huge differences between the finite element results with a mesh size of 1.5 mm and those with the other mesh sizes, as shown in Fig. 7(b). As the mesh size decreases, the impact load history curves tend to be consistent gradually. There is no significant difference between the numerical results with mesh sizes of 0.5 mm and 0.3 mm, so the mesh size of 0.5 mm is selected to balance the calculation accuracy and efficiency.

The cross-section of the 3D-printed projectile in the experiment can only be circular due to the limitation of the launching method. Here, the diameter of the circular cross-section is taken as the length $2a$ of the loading area when the experimental situation is simplified to the two-dimensional loading situation in the theoretical model. However, in the corresponding three-dimensional loading case of the theoretical model, the cross-section shape of the projectile is square, that is, the width of the projectile is equal to the width of the beam, as shown in Fig. 8(a). Therefore, the dynamic response process of the projectiles with circular and square cross-sections impacting an identical flexible beam is compared through finite element simulation to verify the feasibility of this simplified method. The graded cellular projectile with the circular cross-section was generated by cutting the projectile with the square cross-section, as shown in Fig. 8(b). The simulation results show that the velocity history and impact pressure variation under the impact of the projectiles with circular and square cross-sections are almost the same, with only slight differences, as shown in Fig. 9. Therefore, the two-dimensional theoretical model is available for predicting the impact circumstance in the test.

3.2. Preparations of test samples

The fused deposition modeling (FDM) technique was applied to fabricate the graded cellular projectiles pre-designed. A 3D printing machine from Company Stratasys Dimension Elite was employed, as shown in Fig. 10(a), and the ABS plastic was used as the substrate filament material. The density of the ABS plastic is $\rho_s = 966$ kg/m^3, Young's modulus is 1.6 GPa, and the yield stress is $\sigma_{ys} = 42$ MPa. The STL file of the cellular structure can be generated by applying the methods proposed in Wang et al. (2018b) based on the mesostructure design. After pre-processing the STL file, such as slicing, setting printing parameters, and planning tool path, the ABS-based graded cellular projectile can be fabricated by the 3D printer, as shown in Fig. 10(b).

Uniform cellular samples with different relative densities were generated and manufactured by 3D printing to determine the parameters of ABS cellular material in the R–PH model, as shown in Fig. 11. Uniaxial quasi-static compression experiments were
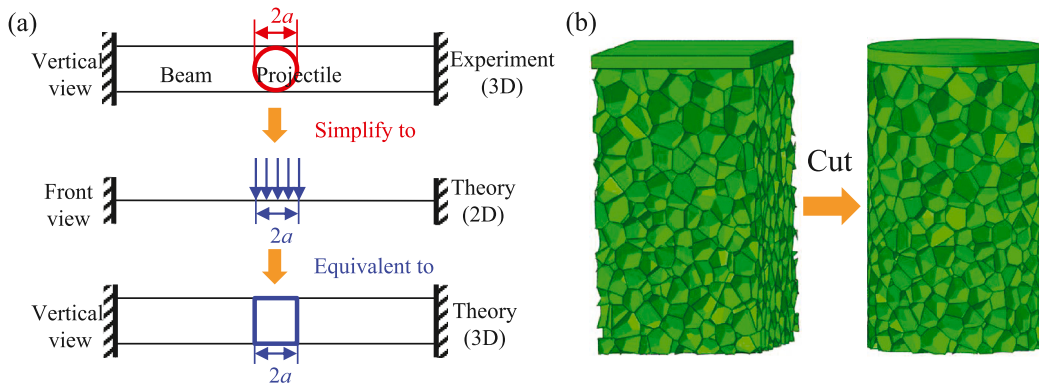
Fig. 8. (a) Equivalent impact situation of the circular projectile and (b) the generation of the circular projectile.
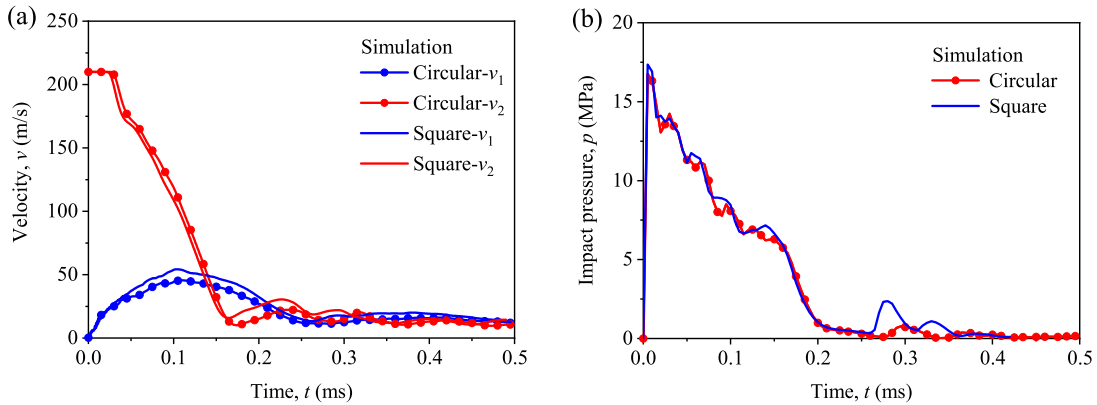

Fig. 9. Time history of the velocity (a) and the impact pressure (b) for circular and square projectiles impacting the same flexible beam.
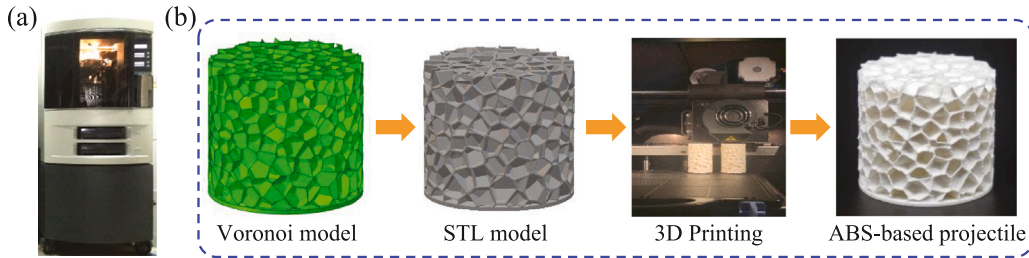

Fig. 10. (a) 3D printing equipment and (b) construction process of graded cellular projectiles.

carried out with a material testing machine MTS 810 at a strain rate of 10^{-3}/s to get the nominal stress–strain curves of 3D-printed ABS cellular material, which are presented in Fig. 12(a). The R–PH model (Zheng et al., 2014) and the statistical model (Wang et al., 2018b) were used to fit the nominal stress–strain data, as shown in Fig. 12(a). Although the fitting effect of the R–PH model is not precise enough as the statistical model, the R–PH model is also in good agreement with the overall trend of the stress–strain curves with fewer parameters, thus the R–PH model is employed to characterize the mechanical properties of the ABS cellular material in this study. The fitting parameters k_1, n_1, k_2, and n_2 in the R–PH model of ABS cellular material were obtained as 1.53, 2.30, 0.30, and 1.89, respectively.

The monolithic beam with a density of ρ_{beam} = 7689 kg/mm^3 was made by wire-cutting 304 stainless steel plate. The uniaxial tensile stress–strain curve of 304 stainless steel was measured quasi-statically at a nominal strain rate of 0.002/s and plotted in Fig. 12(b). By fitting the linear segment of the stress–strain curve, the elastic modulus E of 304 stainless steel is obtained as 191 GPa. The stress at the plastic strain of 0.2% is taken as the yield stress σ_Y, which is 313 MPa. As mentioned before, the strain-rate effect of the stainless-steel was not considered in this study for simplicity. With the increase of the initial momentum of the projectile, i.e., the enhancement of the impact load, the strain-rate sensitivity of the beam may become significant (Radford et al., 2006b; Yang et al., 2018) and should be involved in the design strategy for improving its accuracy.
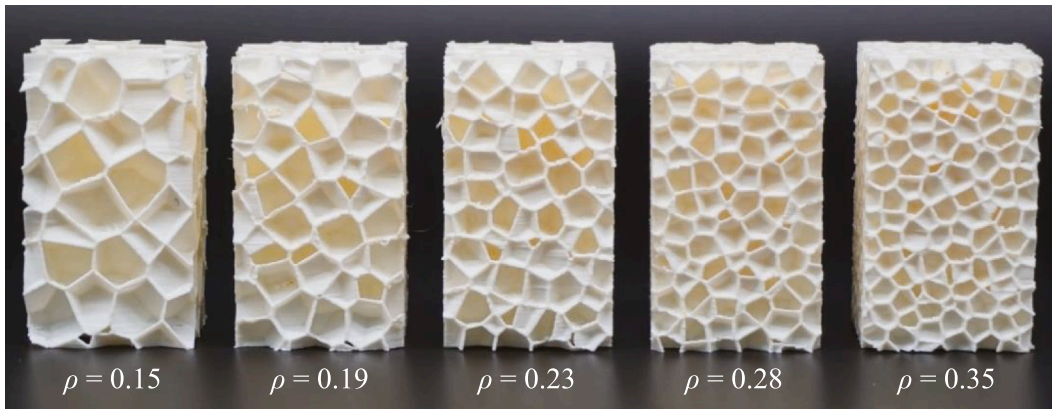
Fig. 11. 3D printed uniform ABS cellular specimens with different relative densities ranging from 0.15 to 0.35.
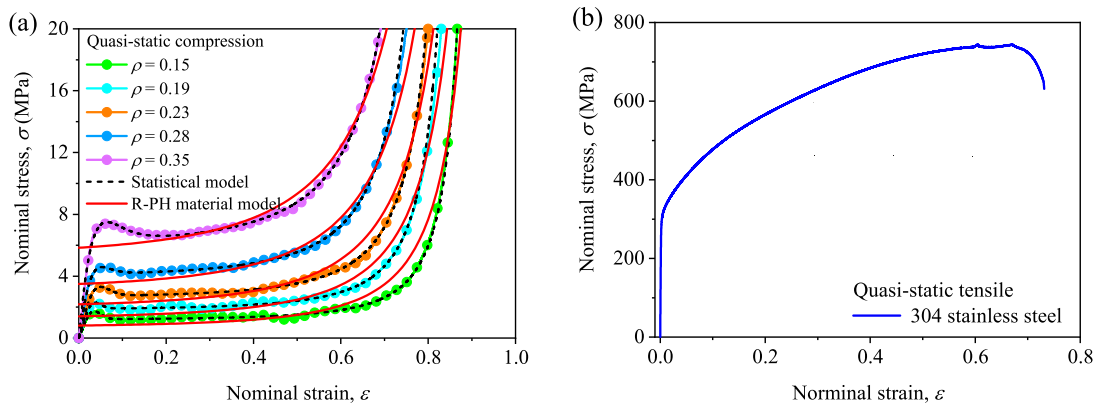

Fig. 12. (a) The nominal stress–strain curves of 3D-printed ABS cellular material under quasi-static compression and the fitting material models, and (b) the tensile stress–strain curve of beam material 304 stainless steel.

3.3. Impact test method

An impact test platform using graded cellular projectiles to realize blast loading was built, as shown in Fig. 13(a). The beam was clamped on a customized fixture to ensure the mid-span of the beam and the barrel axis at the same height, as shown in Fig. 13(b). The deformable length of the beam is 200 mm. The cellular projectile was loaded into the barrel with an inner diameter of 37 mm, and then pushed and accelerated by the nitrogen released from the gas tank. The muzzle velocity V_0 of cellular projectiles was measured by the laser velocimeter at the front end of the gun. The impact process was captured by a high-speed camera (Photron FASTCAM SA5) for further analysis. The shooting frame rate of the high-speed camera is 105000 fps, the pixels of each frame are 128×336, and the pixel-space conversion factor is 0.61 mm/px. The gray images captured by the high-speed camera were binarized to get the binary images of the beam profile. The outline of the beam was extracted from the binary images, and the mathematical expression of the beam profile in each frame was obtained by fitting the outline with a high-order polynomial function, as shown in Fig. 14. Combining with the pixel-space conversion factor, the deflection data of the beam was obtained, and then the velocity data was calculated according to the shooting time interval.

4. Results

4.1. Samples of multiscale design

A blast load with a peak load p_0 of 20 MPa and a decay time constant τ of 0.1 ms is to be simulated through the multiscale design of the graded cellular projectile, as shown in Fig. 15. In the theoretical design, the matrix material of the graded cellular projectile is ABS plastic, and the material of the impacted beam is 304 stainless steel. According to the experimental data, the density ρ_s and the yield stress σ_{ys} of ABS are set as 966 kg/m³ and 42 MPa, and the fitting parameter k_1, n_1, k_2 and n_2 of R–PH model of ABS-based cellular material are 1.53, 2.30, 0.30 and 1.89, respectively. The density ρ_{beam} and yield stress σ_Y of the beam are 7689 kg/m³ and 313 MPa, respectively. The section dimension of the graded cellular projectile is $2a = 36.5$ mm, and the thickness of the monolithic
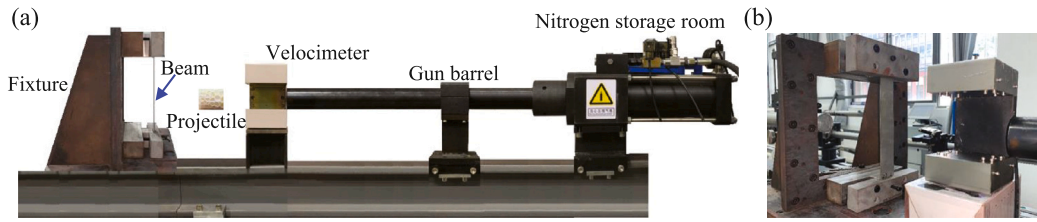
Fig. 13. Loading test platform using graded cellular projectiles to simulate blast loading: (a) schematic diagram of experiment and (b) customized fixture for clamping the tested structure.
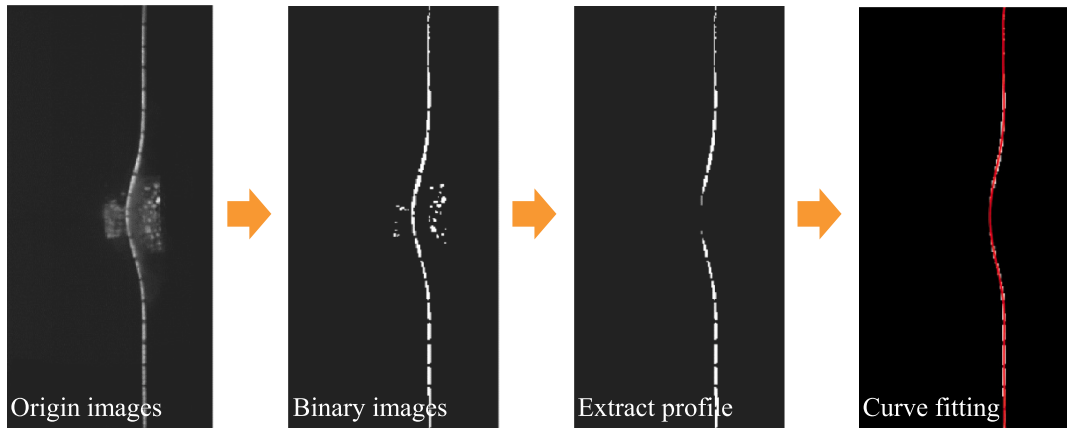

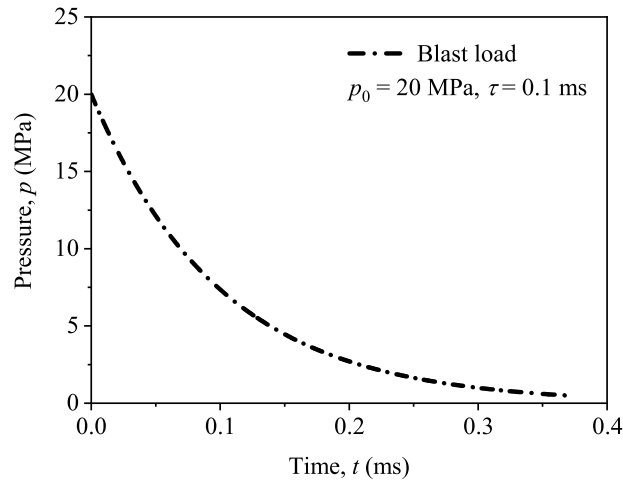**Fig. 14.** Analysis method of high-speed photographic images.

Fig. 15. The blast load $p(t)$ to be simulated by a graded cellular projectile.

beam is $h = 2.5$ mm. The total mass per unit area m_p and the initial velocity V_0 of the graded cellular projectile are needed to be assumed in advance before solving the density distribution of the projectile. Thus, projectiles with different m_p or V_0 are designed and presented below.

For the case that the total mass per unit area m_p of graded cellular projectiles is 0.0095 g/mm², the numerical solutions of the density distribution of the graded cellular projectiles were solved and presented in Fig. 16(a). The mass per unit area m_b of the tail block of three projectiles with the initial velocity V_0 of 170, 180, and 190 m/s are 0.0038, 0.0027, and 0.0013 g/mm², respectively. The relative density ρ_0 at the proximal end of the projectile decreases with the increase of V_0. For $V_0 = 170$ m/s, the density of the projectile increases first and then decreases slightly at the distal end. As the initial velocity increases, the decreasing trend of the density at the distal end of the projectile becomes obvious, the mass of the tail block decreases, and the length of the cellular part
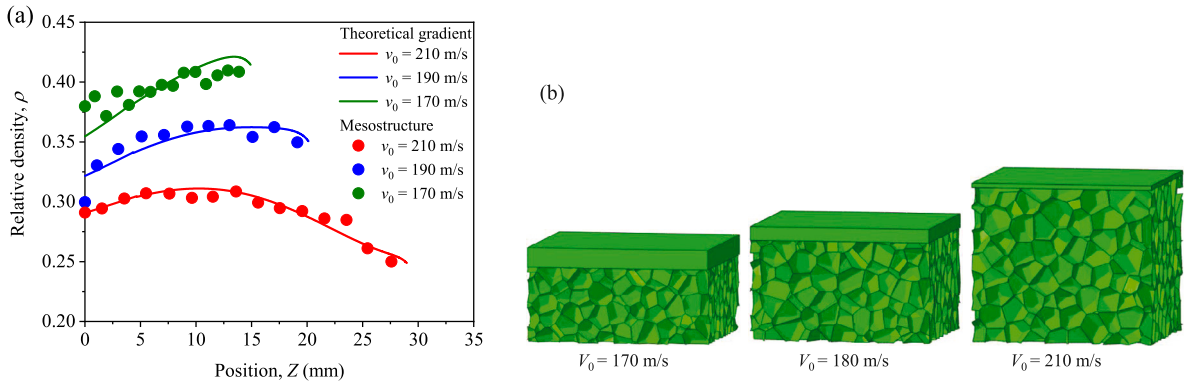
Fig. 16. The multiscale design of graded cellular projectiles with the same total mass per unit area m_p = 0.095 g/mm^2 but different initial velocities V_0: (a) density distribution and (b) mesostructure.
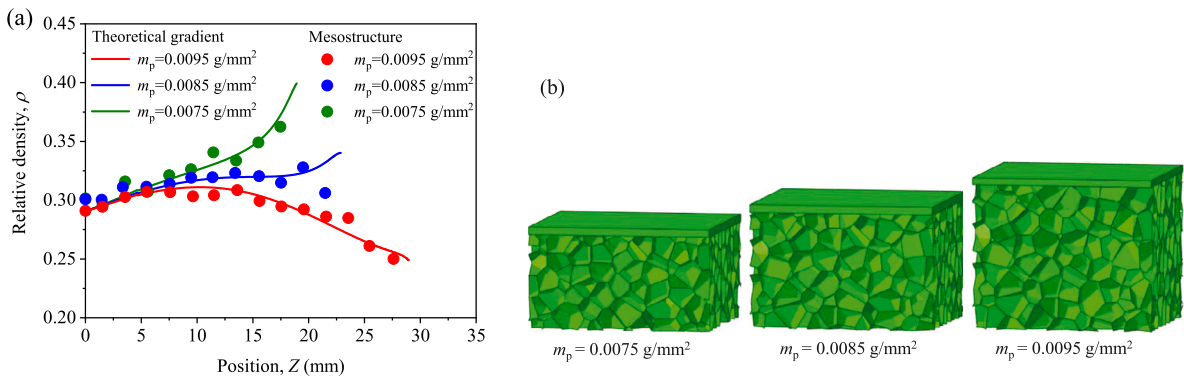

Fig. 17. The multiscale design of graded cellular projectiles with the same initial velocity V_0 = 210 m/s but different total masses per unit area m_p: (a) density distribution and (b) mesostructure.

increases. By using the commended cell parameters h_c = 0.5 mm and k = 0.4, the corresponding mesostructures of graded cellular projectiles are constructed, as shown in Fig. 16(b).

For graded cellular projectiles with the same initial velocity V_0 of 210 m/s but different total mass per unit area m_p of 0.0075, 0.0085, and 0.0095 g/mm^2, their density distribution curves are presented in Fig. 17(a), and the mass of the tail block is 0.00151, 0.00153, and 0.00132 g/mm^2, respectively. The relative densities ρ_0 at the proximal end of the three projectiles remain constant due to the identical value of the initial velocity V_0. For m_p = 0.0075 g/mm^2, the density of the graded cellular projectile increases monotonically. With the increase of m_p, the density distribution changes to first increase and then decrease, the length of the cellular part increases, and the mass change of the tail block is slight. The mesostructures of the projectiles are presented in Fig. 17(b).

4.2. Deformation features

The impact experiment of the graded cellular projectiles was carried out on the test platform introduced in Section 3.2, and the corresponding finite element model was constructed and implemented with ABAQUS/Explicit code. Here, as presented in Section 4.1, the ABS graded cellular projectile with m_p = 0.0095 g/mm^2 and V_0 = 210 m/s designed for the steel beam with a thickness of h = 2.5 mm is prepared and serves as an example for experimental verification. The surface of the monolithic beam is painted black to enhance the contrast between the beam and the white projectile, which is beneficial to image data processing. Similarly, the mass block of the projectile is also painted black to identify its position. The high-speed photographs of the impact process and the deformation process in the finite element simulation are shown in Fig. 18. During impact, two inner plastic hinges are generated near the mid-span of the monolithic beam, and two outer plastic hinges are formed outside the impact area. As the outer plastic hinge moves outwards, the deformation region of the beam expands outward, and the mid-span deflection also increases. The deformation process of the beam in the simulation is identical to that in the experiment, and the deformation mode is consistent with the basic hypothesis of the theoretical design model.

From the deformation process of the graded cellular projectile, it is found that a certain degree of fracture damage occurs, which makes the broken cell-wall material on the exterior surface of the projectile splash out, as shown in Fig. 19(a). Due to the brittleness of the ABS plastic, it is difficult to avoid the fracture of the graded cellular projectile under high-velocity compression (Chang et al.,
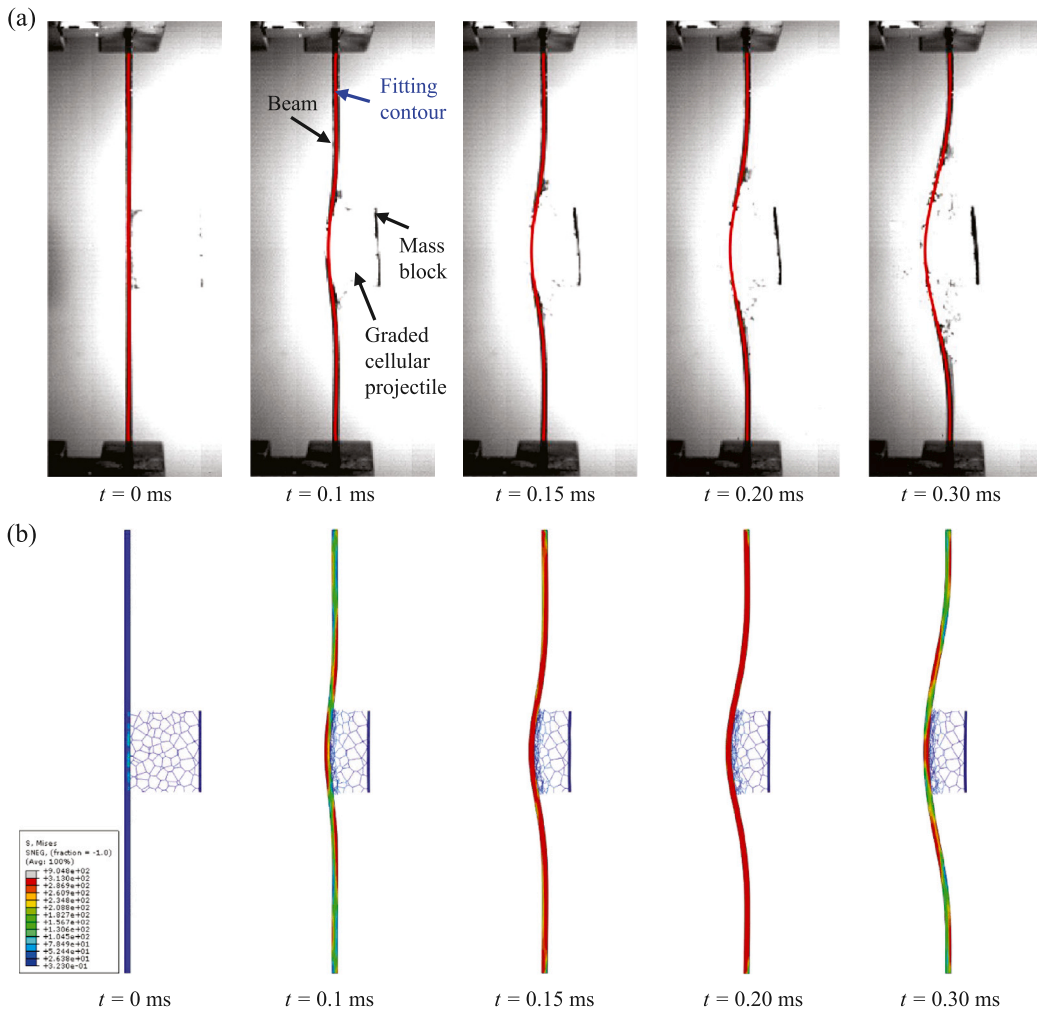
Fig. 18. Deflection variation of the flexible beam in the experiment (a) and simulation (b).

2023), which may make the impact load in the test slightly lower than the blast load since the fragments carry momentum. In the simulation, it can be observed that cells fold and collapse because the fracture characteristics are not considered in the material model. The crushing band is first generated on the proximal end and then propagated from the proximal end to the distal end, as shown in Fig. 19(b). The meso-configuration of the cell was presented by the scanning electron micrographs. A semi-closed cell at a certain position on the proximal end face of the projectile was selected, as shown in Fig. 20(a). The cells at this position were cut from the initial and the impacted projectile and then observed under the electron microscope after pre-processing. Before impact, 3D-printed filaments were stacked in a ladder shape to form the cell-wall, as shown in Fig. 20(b). After impact, although a few filaments were fractured, most of them kept their complete shape and stacked tightly in a plane, as shown in Fig. 20(c). It can be concluded that orderly layer-by-layer crushing is the main deformation mode of the graded cellular projectile, and the finite element simulation can explore the dominant mechanical response mechanism of the cellular material without considering the fracture failure. Therefore, the rationality of the density design method based on the shock wave theory is confirmed. It should be noted that matrix material with good toughness is recommended to reduce the negative effect of fracture and splash of exterior cell-wall materials on the impact load and the experimental observation, and also to reduce the risk of material spallation at the free end of the projectile.

4.3. Impact velocity

The ABS graded cellular projectile with $m_p = 0.0095$ g/mm^2 and $V_0 = 210$ m/s designed for the steel beam with a thickness of $h = 2.5$ mm is taken as an example to carry out the comparison of the velocities obtained from the experimental test, theoretical prediction, and finite element simulation. The mid-span velocity v_1 of the beam and distal velocity v_2 of the graded cellular projectile were obtained through high-speed photographs with the digital image processing method. The coupling analysis model was also
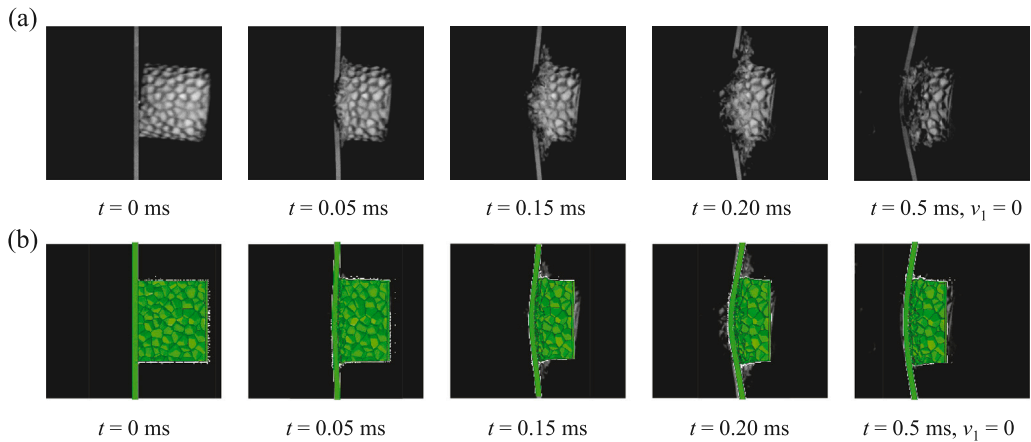
Fig. 19. Deformation of the graded cellular projectile in the experiment (a) and simulation (b).
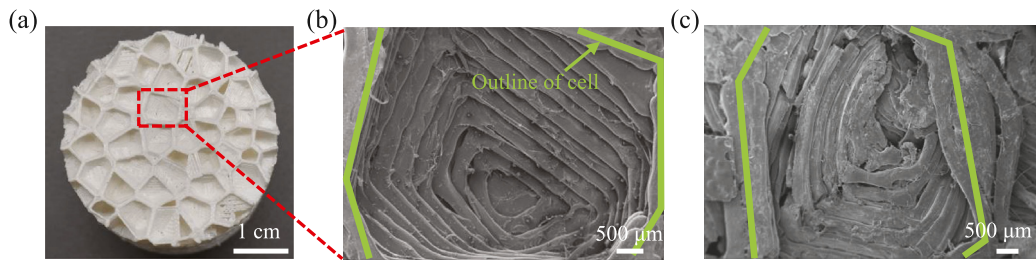

Fig. 20. A cell on the proximal end of the graded cellular projectile: (a) the location of the cell and the scanning electron microscope pictures (b) before impact and (c) after impact.
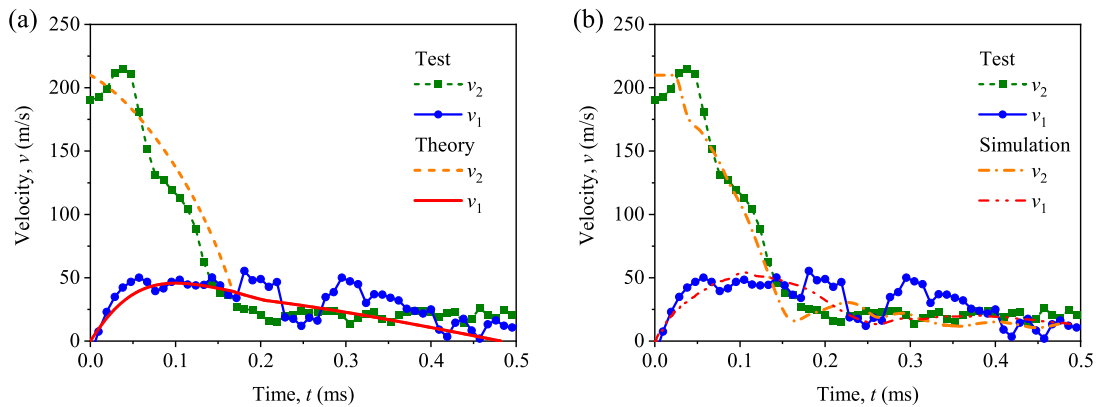

Fig. 21. Comparison of beam mid-span velocity v_1 and projectile tail velocity v_2: (a) test data and theoretical predictions (b) test data and finite element results.

applied to predict the theoretical velocity variations of the graded cellular projectile and the beam. In the finite element simulation, the average velocity of the nodes near the mid-span of the beam (within the 2 mm × 2 mm area centered on the mid-span) is taken as v_1, and the average velocity of the nodes on the distal end of the graded cellular projectile is taken as v_2. As can be seen from Fig. 21(a), the velocity variation of theoretical prediction and experimental test are in good agreement, which declares the reliability of the coupling analysis model. It should be noted that the distal velocity v_2 predicted by the theory is slightly below that of the experimental tests. This is mainly attributed to the fact that the plateau stress of cellular material increases under high-strain rate loading compared with quasi-static loading. Since the strain rate effect is not considered in the theory, the velocity of the undeformed part predicted by the theory decays slightly slower than that of the test. The velocity curves of v_1 and v_2 obtained from the numerical test coincide well with the experimental results, which verify the validity of the finite element simulation and also implies that the influence of material fracture is negligible in this study, as shown in Fig. 21(b).
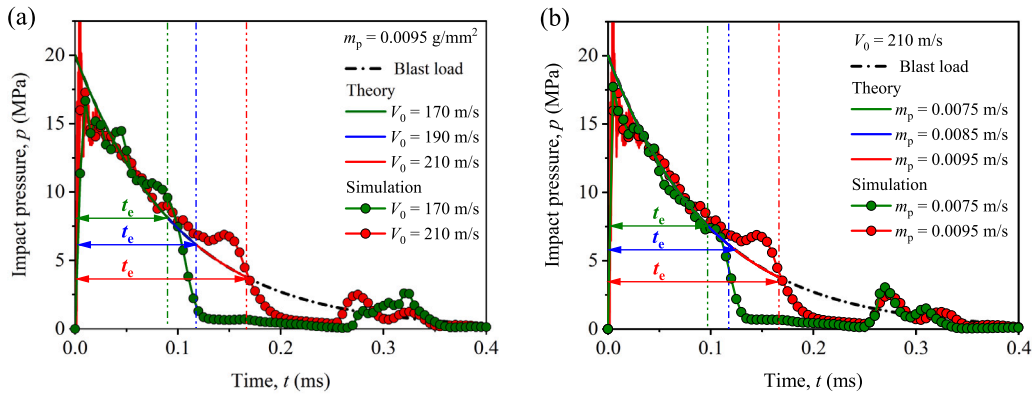
Fig. 22. Impact pressure and simulation effect: (a) Graded cellular projectiles with the same m_p but different V_0, (b) graded cellular projectiles with the same V_0 but different m_p.

4.4. Impact pressure

The impact pressures p of graded cellular projectiles were calculated and compared based on the finite element results. The impact pressure can be obtained by dividing the sum of nodal forces in the loading direction within the loaded region of the beam with the cross-sectional area of the projectile. Here, the increase in the contact area caused by plastic Poisson's ratio is not taken into account. The impact pressure obtained from simulation results and the effective simulation duration t_e predicted by the theory are shown in Fig. 22. The impact pressures produced by graded cellular projectiles with the same m_p of 0.0095 g/mm² but different V_0 of 170 m/s and 210 m/s are in good agreement with the blast loading before 0.09 ms and 0.17 ms, respectively, which is consistent with the effective simulation duration predicted by the theoretical design model, as shown in Fig. 22(a). After the effective simulation time, the impact pressure decays to almost zero rapidly, which implies that the subsequent motion of the crushed part and the attached mass have little influence on the tested structure. Then, the impact pressure rises and oscillates slightly due to the elastic rebound of the beam. Interestingly, when the total mass of the projectile remains unchanged, as the initial velocity increases, the time while the projectile keeps crushing is extended. As a result, the effective simulation time of the projectile increases and the uncrushed mass (the attached mass) decreases. It can be inferred that a lighter attached mass means a better load simulation effect under the premise of the same total mass.

For graded cellular projectiles with the same V_0 of 210 m/s but different m_p, the impact pressure produced by the graded cellular projectile with m_p of 0.0075 g/mm² declines sharply at 0.1 ms, and its effective simulation duration is shorter than that of the projectile with $m_p = 0.0095$ g/mm², as shown in Fig. 22(b). In the numerical and experimental tests, both the mid-span velocity curves of the beam and the impact load curves show no obvious oscillation before the end of impact,as shown in Fig. 21(b) and Fig. 22(b), which proves that the elastic effect of the beam is not significant and has little influence on the impact load of the projectile.

The effective simulation duration t_e increases and the simulation effect of the graded cellular projectile is improved with the increase of the total mass and the initial velocity. However, it should be noted that the initial velocity and total mass of the projectile cannot be increased infinitely, the upper limits will be explored in Section 5.3. To sum up, the graded cellular projectile designed has a superior ability to simulate the blast loading on a flexible target within the effective simulation duration, and the effectiveness of the multiscale design method and the accuracy of the fabrication method have been verified.

5. Discussion

5.1. Comparison of different cellular projectiles

Cellular projectiles with different density designs were constructed, and the impact pressures of different projectiles impacting different targets were compared through finite element simulations. In the design cases of this section, the simulated blast load $p(t)$ and the tested flexible beam are consistent with those studied in Section 4. Assuming that the total mass of the cellular projectiles $m_p = 0.0075$ g/mm² and initial velocity $V_0 = 210$ m/s, the density distributions of the graded cellular projectiles designed for the rigid beam (GCP-0) and flexible beam (GCP-1) considering projectile–target coupling effect are presented in Fig. 23(a). Besides, according to the density distribution range of GCP-0 and GCP-1, uniform cellular projectiles (UCP) with relative densities of 0.2, 0.3, and 0.4 are selected for comparison. The total mass and initial velocities of the uniform cellular projectiles are consistent with those of GCP-0 and GCP-1 to ensure comparability.

The relative densities at the proximal end of GCP-0 and GCP-1 are identical, but their densities behind the proximal end are completely different. The density of GCP-1 increases and the density of GCP-0 decreases first and then increases. Compared with GCP-0, the average density of GCP-1 is greater, and the length is shorter. In the design circumstance of GCP-1, the flexible target has
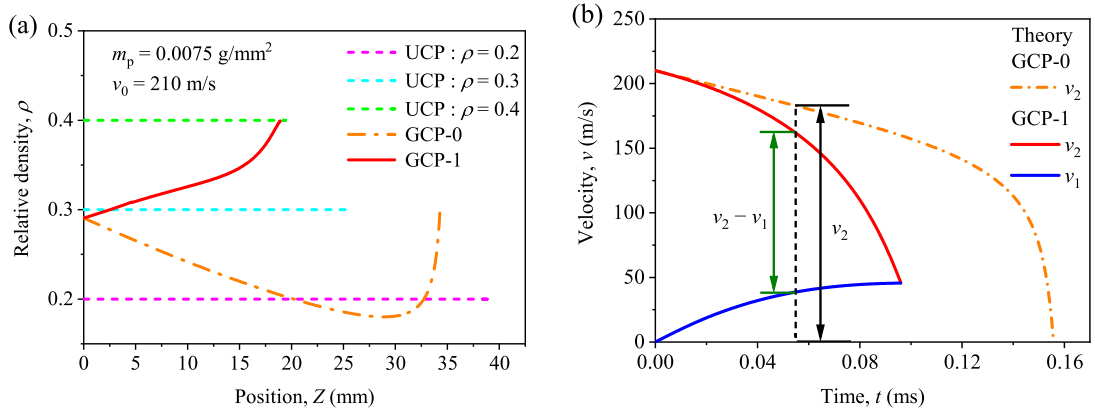
Fig. 23. (a) The density distributions of different cellular projectiles with m_p = 0.0075 g/mm^2 and V_0 = 210 m/s, including UCP, GCP-0, and GCP-1, and (b) the predicted velocities of GCP-0 and GCP-1 before the shock front stop moving under their design circumstances.
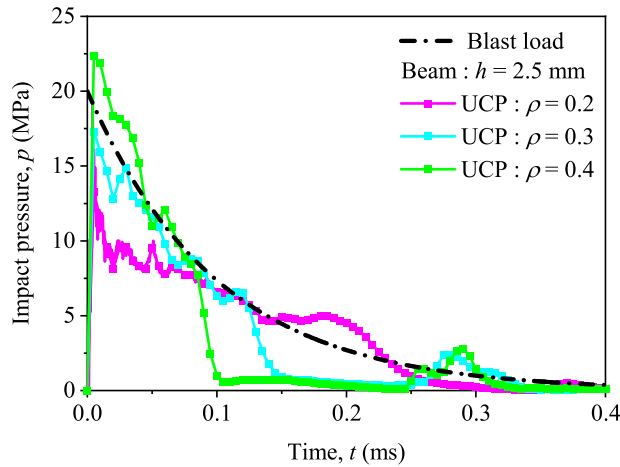

Fig. 24. The impact pressure of UCP with m_p = 0.0075 g/mm^2 and V_0 = 210 m/s but different densities when impacting the beam of h = 2.5 mm.

a moving speed during the impact, while the rigid target is stationary in the design circumstance of GCP-0. Because of the coupling relationship between the velocities of GCP-1 and the flexible target, the velocity difference behind and ahead of the shock front of GCP-1 (i.e., $v_2 - v_1$) decays more than that of GCP-0 (i.e., v_2) at the same moment, and the enhancement of hydrodynamic stress caused by the impact is also weakened, as shown in Fig. 23(b). Therefore, the density of GCP-1 must be greater than that of GCP-0 to achieve a blast-like load.

The impact pressures of UCP with different relative densities when impacting the flexible beam are shown in Fig. 24. The triangular-shaped impact pressures of UCP with relative densities of 0.2 and 0.4 are completely different from the blast load, in which the former is much less than the blast load and lasts longer, while the latter is larger than the blast load and lasts shorter. The impact pressure of UCP with ρ of 0.3 is also less than the blast load. As a result, uniform cellular projectiles cannot simulate the nonlinear attenuation characteristics of the blast loading, which also illustrates the necessity of density design for the cellular projectile.

For the GCP-0, its impact pressure on the rigid target agrees well with the blast loading, but the obvious weakening appears in the impact pressure when it impacts the flexible target, as shown in Fig. 25(a). As the beam thickness h decreases, the impact pressure of the GCP-0 attenuates more. Therefore, when impacting a deformable protective structure, the actual impact pressure formed by the GCP-0 on the target is not consistent with the blast loading due to the projectile–target coupling effect. Similarly, the impact pressure of GCP-1 also changes when the impacted target changes. For example, when the GCP-1 designed considering the target with a thickness of 2.5 mm impacts the target with a thickness of 1.5 mm, the impact pressure of GCP-1 decreases for the strengthening of coupling effect caused by the reduction of structural strength and mass of the target, as shown in Fig. 25(b). This not only proves the necessity of considering the coupling effect in the density design but also indicates that there is a unique correspondence between the application condition and the design condition of the graded cellular projectile.
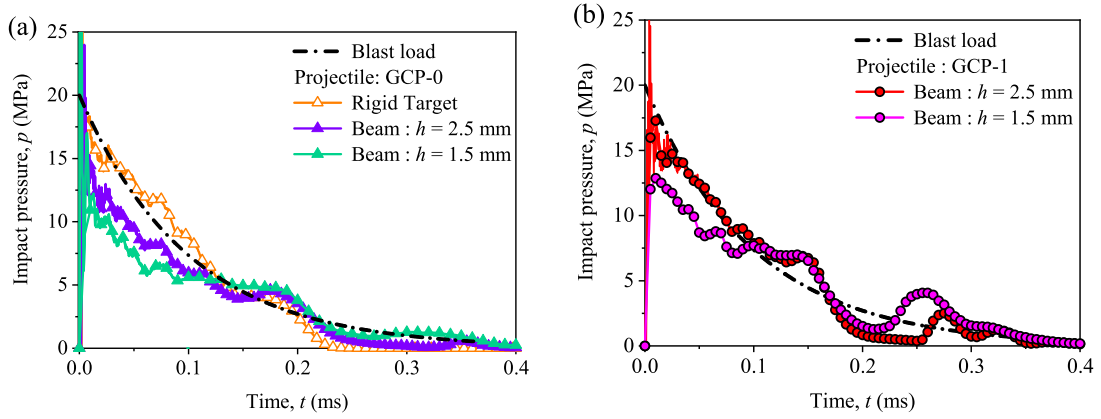
Fig. 25. The impact pressure histories: (a) GCP-0 with $m_p = 0.0075$ g/mm^2 and $V_0 = 210$ m/s when impacting different targets and (b) GCP-1 with $m_p = 0.0095$ g/mm^2 and $V_0 = 210$ m/s when impacting different targets.
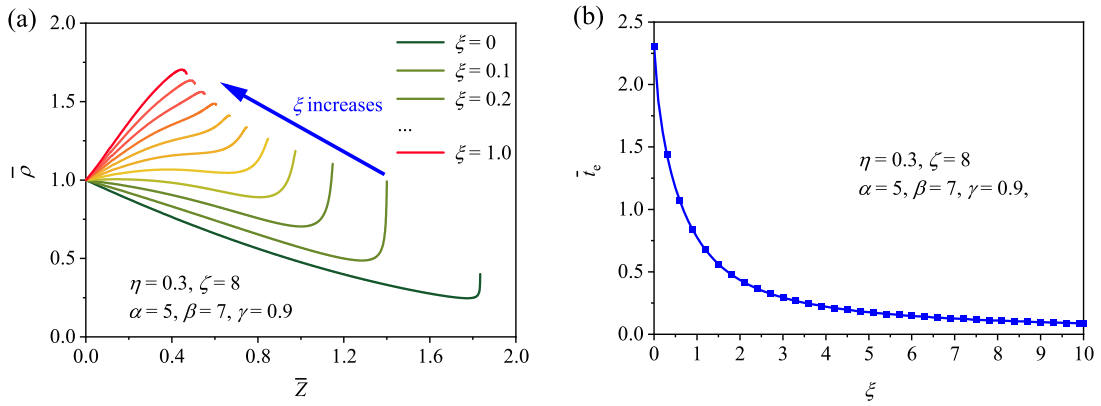

Fig. 26. The influence of the dimensionless parameter ξ: (a) the dimensionless density distribution and (b) the dimensionless effective simulation duration of the graded cellular projectile.

5.2. Effect of coupling parameters

The effects of coupling parameters ξ, η, and ζ on density design and simulation effect are discussed. For the dimensionless parameter ξ, when it tends to 0, i.e., the mass of the flexible beam is far greater than the mass of the graded cellular projectile, the dimensionless governing equations of the density distribution are reduced to

$$\begin{cases} \bar{\rho}^{n_1} + \alpha \bar{\rho} \bar{v}_2 \left(\bar{v}_2 + \dfrac{\beta - \alpha - 1}{\alpha} \sqrt{\bar{\rho}^{n_2 - 1}} \right) = \beta \bar{p} \\ \dfrac{\mathrm{d}\bar{\Phi}}{\mathrm{d}\bar{t}} = \dfrac{\alpha}{\beta \gamma} \left(\bar{v}_2 + \dfrac{\beta - \alpha - 1}{\alpha} \sqrt{\bar{\rho}^{n_2 - 1}} \right) \\ \dfrac{\mathrm{d}\bar{v}_2}{\mathrm{d}\bar{t}} = -\dfrac{\bar{\rho}^{n_1}}{\beta \gamma (1 - \bar{m}_1)}, \quad \bar{m}_1 = \displaystyle\int_0^{\bar{\Phi}} \bar{\rho}(\bar{Z}) \, \mathrm{d}\bar{Z} \end{cases} \tag{54}$$

which is equivalent to the dimensionless governing equations in the case of a graded cellular projectile impacting a rigid beam. We consider the case that $\alpha = 5$, $\beta = 7$, $\gamma = 0.9$, $\eta = 0.3$, and $\zeta = 8$. When ξ gradually increases from 0, i.e., the mass of the beam decreases relatively, the rigidity of the target is weakened, and the influence of the projectile–target coupling effect is gradually enhanced. It can be found that with the increase of ξ, the dimensionless density distribution of the graded cellular projectile transit from the trend of first decreasing and then increasing to increasing all along, the dimensionless length of the projectile decreases, as shown in Fig. 26(a). With a large value of ξ, the projectile and the beam will reach the common velocity quickly, the crushing process of the projectile is short or even difficult to happen, and thus the dimensionless effective simulation duration $\bar{t}_e$ of the graded cellular projectile decreases, as shown in Fig. 26(b). Therefore, the lower the mass of the anti-blast material or structure, the worse the effect of the graded cellular projectile on simulating the blast loading. The mass ratio ξ should preferably be less than 0.5 to exert the testing ability of the graded cellular projectile.

The dimensionless parameter η means the moment ratio of the beam and the simulated blast loading. In the research scope of interest in this study, the deformation of the target is considered to make the projectile–target coupling effect involved, so the peak pressure p_0 of the simulated blast load must be larger than the static collapse pressure p_c of the target. The static collapse pressure p_c of a clamped monolithic beam can be obtained from the upper bound theorem (Jones, 2011) as

$$p_c = \frac{4M_0}{a(2l - a)} = \frac{\sigma_Y h^2}{a(2l - a)}. \tag{55}$$

As mentioned before, the physical quantity — length l is considered to be much longer than the loading patch size a. Referring to the critical conditions $l \geq 2a$ proposed by Qiu et al. (2005), the static collapse pressure p_c is supposed to satisfy

$$p_c \leq \frac{\sigma_Y h^2}{3a^2}, \tag{56}$$

and the peak load p_0 of the simulated blast load should be larger than the maximum value of p_c, i.e.,

$$p_0 \geq \frac{\sigma_Y h^2}{3a^2}. \tag{57}$$

Hence, the range of the strength ratio is $\eta \leq 3$.

Consider the case $\alpha = 5$, $\beta = 7$, $\gamma = 0.9$, $\xi = 0.3$, $\zeta = 8$, and η changes from 0.001 to 3.0. With the increase of η, the dimensionless length of the projectile increases, and the dimensionless relative density changes from increasing to first decreasing and then increasing, as shown in Fig. 27(a). When the blast loading is far greater than the plastic bending moment of the beam, i.e., the strength ratio η approaches 0 (η is between 0.001 and 0.1), the dimensionless density distribution $\bar{\rho}$ and the dimensionless effective simulation duration $\bar{t}_e$ keeps unchanged. In this case, the inner plastic hinges of the beam do not reach the mid-span when the shock front in the projectile stop propagating. From the governing equations of Stage I, the strength ratio η only affects the moving speed of the outer and inner hinges, and the physical quantities directly related to the density distribution and simulation duration are not influenced by the change of η. With the further increase of η, the inner hinges can reach the mid-span of the beam, and the design process is at Stage II. During Stage II, the strength ratio η affects the deceleration of the deformed portion, thus directly affecting the density distribution of the projectile. For $\eta > 2$, the dimensionless density distribution is not changed remarkably, the dimensionless effective simulation duration of the projectile increases, and the increasing trend steadily decelerates, as shown in Fig. 27(b). When $\eta \to 3$, the effective simulation duration $\bar{t}_e \to 2$. The simulation effect of the graded cellular projectile improves when the strength of the protective structure is enhanced or the simulated load and the loading area decrease. However, when the structural strength increases or the loading area decreases to a certain extent, their influence are no longer significant.

The dimensionless parameter ζ presents the ratio of the flying distance of the projectile within the time scale of the blast loading to the beam thickness. The effects of the dimensionless parameter ζ on the dimensionless density distribution and the effective simulation duration are shown in Fig. 28. For the case of $\zeta = 1$, the dimensionless density distribution curve of the projectile remains almost constant at first and then rises rapidly. With the increase of ζ, the overall trend of the dimensionless density distribution turns into a trend of decreasing first and then increasing, as shown in Fig. 28(a). As ζ increases from 1 to 50, the dimensionless effective simulation duration $\bar{t}_e$ of the projectile increases steadily from 1.25 to 1.75, as shown in Fig. 28(b). Compared with the dimensionless parameters ξ and η, the dimensionless effective simulation duration $\bar{t}_e$ is less sensitive to the change of ζ. Therefore, the value of ζ can be selected in a wide range of 1 to 50, which covers the most reasonable impact circumstances.

The tested protective structure and the simulated blast load codetermine the simulation effect of the graded cellular projectile. Based on the above analysis, when the coupling effect is weaker, that is, the mass is bigger and the strength of the protective structure is stronger, the simulation effect of the graded cellular projectile is better. Therefore, the graded cellular projectile can be widely applied in the anti-blast test of the protective structure since most effective anti-blast structures usually have a large mass and high strength.

5.3. Effect of target-independent parameters

The dimensionless parameter α presents the ratio of the hydrodynamic pressure to the static initial crushing stress of the cellular material at the proximal end of the projectile, which is also named the dynamic–static stress ratio in this study. Replacing σ_{i0} in the definition formula of α with $\sigma_{i0} = k_1 \sigma_{ys} \rho_0^{n_1}$, we have

$$\alpha = \frac{\rho_s V_0^2}{k_1 \sigma_{ys} \rho_0^{n_1 - 1}}, \tag{58}$$

which indicates that the dynamic–static stress ratio α is larger, and the projectile would be more compacted during impact when the yield stress of the base material and the relative density of the projectile at the proximal end are less (or the density of the base material and the initial velocity of the projectile are larger). Parameter β represents the relative value of the blast peak pressure to the initial crushing stress at the proximal end of the projectile, which is also called the load ratio. According to Eq. (45), it can be inferred that this formula is meaningful only when $\beta > 1$ because α must be greater than 0, which provides an understanding that the peak value of the blast loading must be greater than its initial crushing stress at the proximal end. According to Eq. (45), the dimensionless parameters α and β can be expressed by each other as

$$\alpha = \left(\sqrt{\beta - 1 + \frac{k_2}{4k_1} \rho_0^{n_2 - n_1}} - \sqrt{\frac{k_2}{4k_1} \rho_0^{n_2 - n_1}} \right)^2 \tag{59}$$
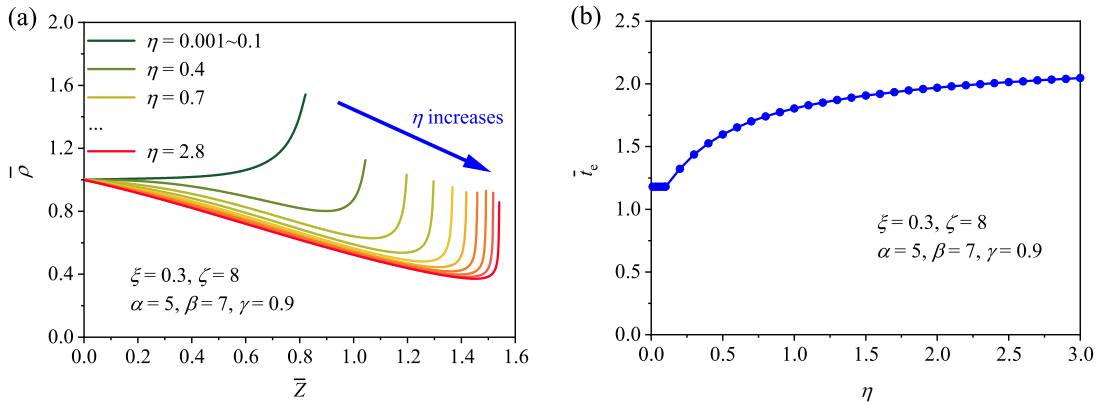
Fig. 27. The influence of dimensionless parameter η: (a) the dimensionless density distribution and (b) the dimensionless effective simulation duration of the graded cellular projectile.

Fig. 28. The influence of dimensionless parameter ζ: (a) the dimensionless density distribution and (b) the dimensionless effective simulation duration of the graded cellular projectile.
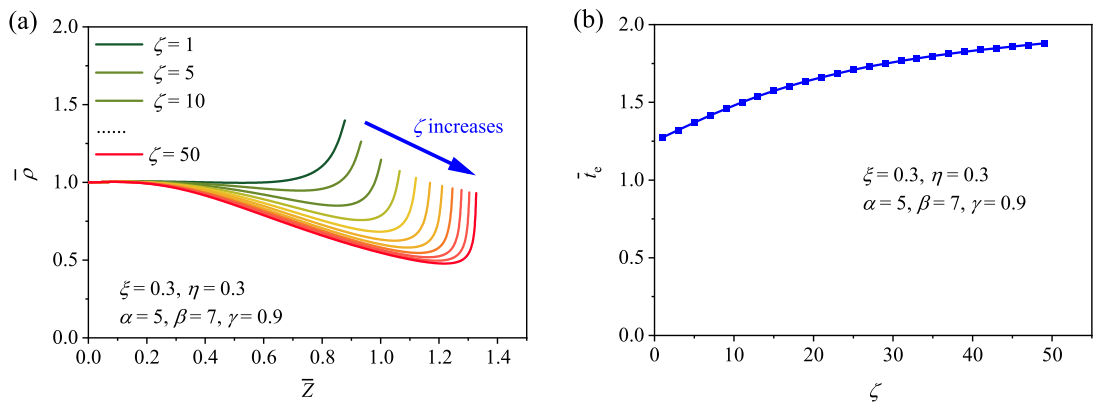
and

$$\beta = \alpha + 1 + \sqrt{\frac{k_2}{k_1} \rho_0^{n_2 - n_1} \alpha}, \tag{60}$$

respectively. By referring to Eq. (59), for a specific cellular material with known material parameters, i.e., k_1, n_1, k_2, and n_2, the range of the dynamic–static stress ratio α can be obtained based on the known value of load ratio β since the relative density of cellular materials is usually between 0.05 and 0.5. In the same way, the appropriate range of the load ratio β can be obtained through Eq. (60) when the dynamic–static stress ratio α is determined. There is a positive correlation between α and β.

Assuming that $\beta = 7$, $\gamma = 0.8$, $\xi = 0.3$, $\eta = 0.3$, and $\zeta = 8$, the reasonable value range of α is determined according to Eq. (59). With increasing α, the overall dimensionless relative density of the graded cellular projectile increases, and $\bar{\rho}$ at the proximal and distal ends of the projectile remains constant, as shown in Fig. 29(a). When γ, ξ, η, and ζ remain unchanged, and $\alpha = 5$, the rational range of β is obtained according to Eq. (60). Contrary to the influence of α, the overall dimensionless density curve with a large β is below that with a small β, as shown in Fig. 29(b). Besides, $\bar{\rho}$ at the distal end increases as β increases. The dynamic–static stress ratio α and the load ratio β only characterize the initial state of the graded cellular projectile and the blast loading, therefore $\bar{t}_e$ of the graded cellular projectile is not influenced by the variation of α and β. The peak load and the density distribution of the projectile can be controlled by adjusting the values of α and β.

It should be noted that the phenomenon of double shock wave (Wang et al., 2013b; Shen et al., 2013) may appear in the graded cellular projectile when α and β are too small. Consider the case of $\alpha = 1$, $\beta = 2.5$, $\gamma = 0.95$, $\xi = 0.5$, $\eta = 0.3$, and $\zeta = 8$, the density distribution at the tail part of the projectile shows a large negative gradient. The stress field of the projectile at each moment is calculated based on Newton's second law, as shown in Fig. 30. From $\bar{t} = 0.2$, the stress distribution of the projectile at the distal end is higher than its local initial crushing stress, which conflicts with the single wave hypothesis we proposed in the theoretical design model. The small value of α indicates that within the impact pressure composed of the hydrodynamic pressure $\rho_s \rho_0 V_0^2$ and the initial crushing stress σ_{i0}, the former is relatively weak, and the latter plays the main role. Therefore, the initial crushing stress
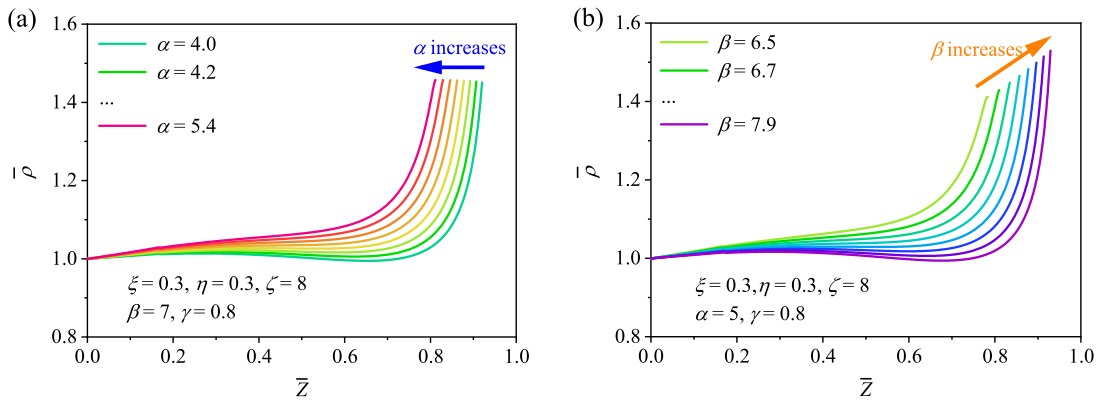
Fig. 29. (a) The influence of dimensionless parameter α on the dimensionless density, (b) the influence of dimensionless parameter β on the dimensionless density.
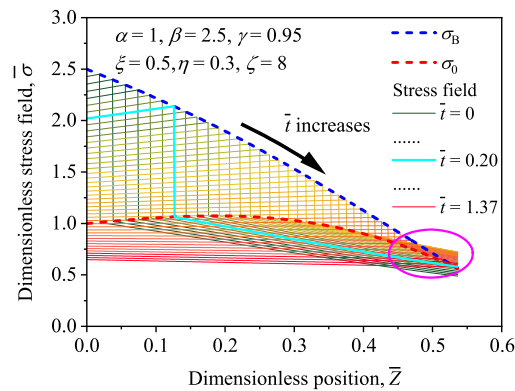

Fig. 30. Stress field evolution of the graded cellular projectile during crushing.

of the distal part of the projectile has to decline drastically, that is, the relative density has to decrease significantly to achieve the attenuation of the impact pressure in the later stage. In summary, the density with the characteristic of a large negative gradient should be avoided, and small values of α and β (say, < 2), are not recommended in the design of the graded cellular projectile.

The impulse–time relation of the blast loading can be obtained by integrating its load–time function as

$$I(t) = \int_0^t p_0 e^{-t/\tau} \mathrm{d}t = p_0 \tau \left(1 - e^{-t/\tau}\right). \tag{61}$$

The total impulse of the blast loading is $p_0\tau$ when $t \to \infty$. Therefore, the dimensionless parameter γ is the ratio of the initial momentum of the graded cellular projectile to the total impulse of the simulated blast load. Considering the case of $\alpha = 5$, $\beta = 7$, $\xi = 0.3$, $\eta = 0.3$, and $\zeta = 8$, the dimensionless density distribution of the graded cellular projectile with $\gamma = 0.2$ increases monotonically. As γ changes from 0.2 to 1.1, the density curves of the projectile gradually turn into a trend of increasing first and then decreasing, as shown in Fig. 31(a). Meanwhile, $\bar{t}_e$ of the projectile rises with the increase of γ, as shown in Fig. 31(b). For a specific simulated blast load, the increase of γ implies the increase in the initial momentum of the projectile. When the initial momentum increases, the crushing process of the graded cellular projectile is prolonged, which leads to the increase of $\bar{t}_e$. This finding also explains the phenomenon discovered by Radford et al. (2005) that the length, density, and initial velocity of the uniform cellular projectile have a significant influence on its impulse duration, which is essentially due to the change of the initial momentum caused by the change of these physical quantities. However, it should be noted that $\bar{\rho}$ at the distal end of the projectile approaches 0 when $\gamma = 1.1$, which is contrary to the single wave hypothesis and unable to be manufactured in the reality, as shown in Fig. 31(a). As mentioned before, with the increase of initial momentum, the effective simulation duration of the graded cellular projectile increases, and the impulse acting on the target transformed from the momentum also increases. When $\gamma > 1$, i.e., the initial momentum of the projectile is greater than the total impulse of the blast loading, and the relative density at the distal end of the projectile is limited to 0 because the blast loading approaches 0 in the later period. As a result, γ should not be greater than 1 to ensure the rationality and realizability of the design. To sum up, under the premise of not exceeding 1, a larger value of γ can help to improve the simulation effect of the graded cellular projectile.
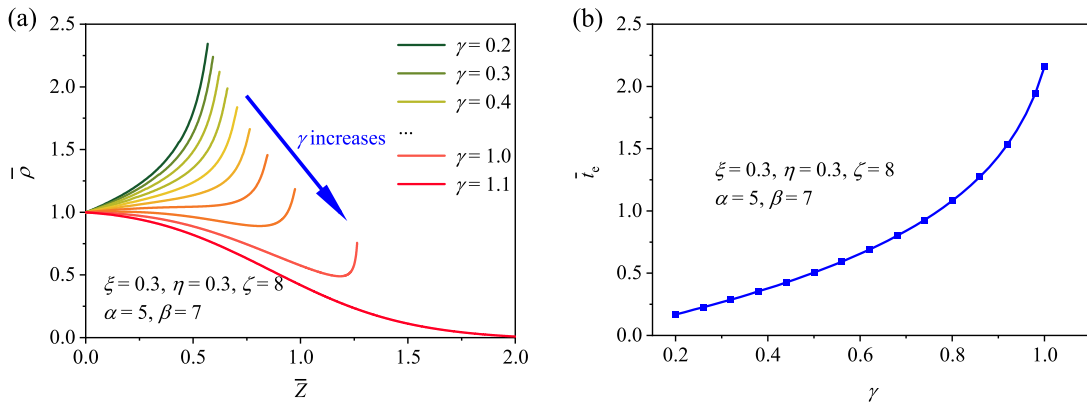
Fig. 31. The influence of dimensionless parameter γ on (a) the dimensionless density distribution and (b) the dimensionless effective simulation duration of the projectile.

6. Conclusions

A multiscale design strategy of graded cellular projectiles considering the projectile–target coupling effect is proposed to simulate blast loading. Combining the shock wave model of the graded cellular projectile and the plastic hinge model of the clamped beam, we obtained the density design governing equations of graded cellular projectiles. The mesostructures of projectiles were constructed using the 3D Voronoi technique and a variable cell-size distribution method, and samples were prepared by 3D printing technology.

For a given blast load and an impacted beam, graded cellular projectiles with different masses and initial velocities were designed and analyzed, and the impact processes of the graded cellular projectiles were studied by numerical simulations and experimental tests. The velocities of the projectiles and the beam predicted by the theoretical model and numerical simulations coincide well with the experimental results. The impact pressure of the graded cellular projectile acting on the flexible beam in the numerical simulations shows good agreement with the blast load. Besides, graded cellular projectiles were designed when considering the rigid and the flexible beams, and their simulation effects of impact load were compared by numerical simulations. The impact pressures on the flexible target generated by the projectile designed without considering the coupling effect are different from the blast loading. These findings indicate the effectiveness of the multiscale design strategy and the necessity of considering the projectile–target coupling effect in the design.

The dimensionless governing equations of density design containing two types of dimensionless parameters, i.e., target-independent parameters and coupling parameters, are obtained. The application situation and the initial parameters selection method of the graded cellular projectile are analyzed through the dimensionless parameters. It is found that with the enhancement of the mass and strength of the target, the effective simulation duration of the projectile increases, and the projectile is more suitable for impact testing for the target. With the relative increase of the initial momentum, the effective simulation duration of the projectile increases. However, to ensure the rationality of the density design, the initial momentum of a projectile cannot exceed the total impulse of the blast load.

In summary, through accurate design and precise preparation, graded cellular projectiles that can simulate the blast loading on the flexible target were presented in this study, which provides a simple, safe, and effective way for exploring the anti-blast properties of protective structures. In further study, the multiscale design strategy can be extended to design the graded cellular projectile impacting the sandwich structure. Based on the design framework we proposed, the accurate yield locus of the tested structure and the strain-rate effects of materials of the projectile and the tested structure can be involved in the theory to improve the accuracy of density design. Besides, blast load with high intensity may be achieved by designing and preparing graded cellular projectiles with metal-based material.

CRediT authorship contribution statement

Yuanrui Zhang: Investigation, Methodology, Software, Validation, Formal analysis, Writing – original draft. **Yudong Zhu:** Investigation, Formal analysis, Writing – review & editing. **Baixue Chang:** Validation, Funding acquisition, Writing – review & editing. **Jilin Yu:** Supervision, Writing – review & editing. **Zhijun Zheng:** Conceptualization, Methodology, Formal analysis, Supervision, Writing – review & editing, Project administration, Funding acquisition.

Declaration of competing interest

The authors declare that they have no known competing financial interests or personal relationships that could have appeared to influence the work reported in this paper.

Data availability

Data will be made available on request.

Acknowledgments

This work is supported by the National Natural Science Foundation of China (11872360 and 12102429). We acknowledge the computer time provided by the Supercomputing Center of University of Science and Technology of China.

References

Aleyaasin, M., Harrigan, J.J., Reid, S.R., 2015. Air-blast response of cellular material with a face plate: An analytical–numerical approach. Int. J. Mech. Sci. 91, 64–70. http://dx.doi.org/10.1016/j.ijmecsci.2014.03.027.

Aune, V., Fagerholt, E., Langseth, M., Børvik, T., 2016. A shock tube facility to generate blast loading on structures. Int. J. Prot. Struct. 7 (3), 340–366. http://dx.doi.org/10.1177/2041419616666236.

Banhart, J., 2001. Manufacture, characterisation and application of cellular metals and metal foams. Prog. Mater. Sci. 46 (6), 559–632. http://dx.doi.org/10.1016/S0079-6425(00)00002-5.

Børvik, T., Olovsson, L., Hanssen, A., Dharmasena, K., Hansson, H., Wadley, H., 2011. A discrete particle approach to simulate the combined effect of blast and sand impact loading of steel plates. J. Mech. Phys. Solids 59 (5), 940–958. http://dx.doi.org/10.1016/j.jmps.2011.03.004.

Chang, B.X., Zheng, Z.J., Zhang, Y.R., Zhang, Y.L., Zhao, K., Yu, J.L., 2023. Crashworthiness design of graded cellular materials: Experimental verification of the backward design strategy. Int. J. Impact Eng. 171, 104366. http://dx.doi.org/10.1016/j.ijimpeng.2022.104366.

Chang, B.X., Zheng, Z.J., Zhang, Y.L., Zhao, K., He, S.Y., Yu, J.L., 2020. Crashworthiness design of graded cellular materials: An asymptotic solution considering loading rate sensitivity. Int. J. Impact Eng. 143, 103611. http://dx.doi.org/10.1016/j.ijimpeng.2020.103611.

Chen, Y., Chen, F., Zhang, W., Du, Z.P., Hua, H.X., 2016. Transient underwater shock response of sacrificed coating with continuous density graded foam core. Composites B 98, 297–307. http://dx.doi.org/10.1016/j.compositesb.2016.05.033.

Conroy, M.F., 1964. The plastic deformation of built-in beams due to distributed dynamic loading. J. Appl. Mech. 31 (3), 507–514. http://dx.doi.org/10.1115/1.3629669.

Duarte, I., Banhart, J., 2000. A study of aluminium foam formation—kinetics and microstructure. Acta Mater. 48 (9), 2349–2362. http://dx.doi.org/10.1016/S1359-6454(00)00020-3.

Espinosa, H.D., Lee, S., Moldovan, N., 2006. A novel fluid structure interaction experiment to investigate deformation of structural elements subjected to impulsive loading. Exp. Mech. 46, 805–824. http://dx.doi.org/10.1007/s11340-006-0296-7.

Fischer, S., Schüler, P., Fleck, C., Bührig-Polaczek, A., 2013. Influence of the casting and mould temperatures on the (micro) structure and compression behaviour of investment-cast open-pore aluminium foams. Acta Mater. 61 (14), 5152–5161. http://dx.doi.org/10.1016/j.actamat.2013.04.069.

Fleck, N., Deshpande, V., 2004. The resistance of clamped sandwich beams to shock loading. J. Appl. Mech. 71 (3), 386–401. http://dx.doi.org/10.1115/1.1629109.

Freidenberg, A., Aviram, A., Stewart, L., Whisler, D., Kim, H., Hegemier, G., 2014. Demonstration of tailored impact to achieve blast-like loading. Int. J. Impact Eng. 71, 97–105. http://dx.doi.org/10.1016/j.ijimpeng.2014.04.006.

Gan, E.C.J., Remennikov, A., Ritzel, D., 2021. Investigation of trees as natural protective barriers using simulated blast environment. Int. J. Impact Eng. 158, 104004. http://dx.doi.org/10.1016/j.ijimpeng.2021.104004.

Gan, E.C.J., Remennikov, A., Ritzel, D., Uy, B., 2020. Approximating a far-field blast environment in an advanced blast simulator for explosion resistance testing. Int. J. Prot. Struct. 11 (4), 468–493. http://dx.doi.org/10.1177/2041419620911133.

He, S.Y., Lv, Y.N., Chen, S.T., Dai, G., Liu, J.G., Huo, M.K., 2020. Gradient regulation and compressive properties of density-graded aluminum foam. Mater. Sci. Eng. A 772, 138658. http://dx.doi.org/10.1016/j.msea.2019.138658.

He, S.Y., Zhang, Y., Dai, G., Jiang, J.Q., 2014. Preparation of density-graded aluminum foam. Mater. Sci. Eng. A 618, 496–499. http://dx.doi.org/10.1016/j.msea.2014.08.087.

Huang, R., Ma, S., Zhang, M., Xu, J., Wang, Z., 2019. Dynamic deformation and failure process of quasi-closed-cell aluminum foam manufactured by direct foaming technique. Mater. Sci. Eng. A 756, 302–311. http://dx.doi.org/10.1016/j.msea.2019.04.050.

Jing, L., Wang, Z., Ning, J., Zhao, L., 2011. The dynamic response of sandwich beams with open-cell metal foam cores. Composites B 42 (1), 1–10. http://dx.doi.org/10.1016/j.compositesb.2010.09.024.

Jones, N., 2011. Structural Impact. Cambridge University Press.

Latourte, F., Gregoire, D., Zenkert, D., Wei, X., Espinosa, H.D., 2011. Failure mechanisms in composite panels subjected to underwater impulsive loads. J. Mech. Phys. Solids 59 (8), 1623–1646. http://dx.doi.org/10.1016/j.jmps.2011.04.013.

Li, L., Han, B., He, S.Y., Zhao, Z.Y., Zhang, R., Zhang, Q.C., Lu, T.J., 2019. Shock loading simulation using density-graded metallic foam projectiles. Mater. Des. 164, 107546. http://dx.doi.org/10.1016/j.matdes.2018.107546.

Li, L., Xue, P., Luo, G., 2016. A numerical study on deformation mode and strength enhancement of metal foam under dynamic loading. Mater. Des. 110, 72–79. http://dx.doi.org/10.1016/j.matdes.2016.07.123.

Liu, J., Hou, B., Lu, F., Zhao, H., 2015. A theoretical study of shock front propagation in the density graded cellular rods. Int. J. Impact Eng. 80, 133–142. http://dx.doi.org/10.1016/j.ijimpeng.2015.02.001.

Martin, J.B., Symonds, P.S., 1966. Mode approximations for impulsively-loaded rigid-plastic structures. J. Eng. Mech. Div. 92 (5), 43–66. http://dx.doi.org/10.1061/JMCEA3.0000787.

Murr, L., Gaytan, S., Medina, F., Martinez, E., Martinez, J., Hernandez, D., Machado, B., Ramirez, D., Wicker, R., 2010. Characterization of Ti–6Al–4V open cellular foams fabricated by additive manufacturing using electron beam melting. Mater. Sci. Eng. A 527 (7–8), 1861–1868. http://dx.doi.org/10.1016/j.msea.2009.11.015.

Ngo, T., Mendis, P., Gupta, A., Ramsay, J., 2007. Blast loading and blast effects on structures – an overview. Electron. J. Struct. Eng. (1), 76–91. http://dx.doi.org/10.56748/ejse.671.

Nian, W., Subramaniam, K.V., Andreopoulos, Y., 2012. Dynamic compaction of foam under blast loading considering fluid–structure interaction effects. Int. J. Impact Eng. 50, 29–39. http://dx.doi.org/10.1016/j.ijimpeng.2012.06.005.

Qin, Q.H., Wang, T.J., 2009. A theoretical analysis of the dynamic response of metallic sandwich beam under impulsive loading. Eur. J. Mech. A Solids 28, 1014–1025. http://dx.doi.org/10.1016/j.euromechsol.2009.04.002.

Qin, Q.H., Wang, T.J., Zhao, S.Z., 2009. Large deflections of metallic sandwich and monolithic beams under locally impulsive loading. Int. J. Mech. Sci. 51 (11–12), 752–773. http://dx.doi.org/10.1016/j.ijmecsci.2009.08.008.

Qin, Q.H., Yuan, C., Zhang, J., Wang, T.J., 2014. A simplified analytical model for metal sandwich beam with soft core under impulsive loading over a central patch. Int. J. Impact Eng. 74, 67–82. http://dx.doi.org/10.1016/j.ijimpeng.2014.06.008.

Qiu, X., Deshpande, V.S., Fleck, N.A., 2003. Finite element analysis of the dynamic response of clamped sandwich beams subject to shock loading. Eur. J. Mech. A Solids 22, 801–814. http://dx.doi.org/10.1016/j.euromechsol.2003.09.002.

Qiu, X., Deshpande, V.S., Fleck, N.A., 2005. Impulsive loading of clamped monolithic and sandwich beams over a central patch. J. Mech. Phys. Solids 53 (5), 1015–1046. http://dx.doi.org/10.1016/j.jmps.2004.12.004.

Radford, D.D., Deshpande, V.S., Fleck, N.A., 2005. The use of metal foam projectiles to simulate shock loading on a structure. Int. J. Impact Eng. 31, 1152–1171. http://dx.doi.org/10.1016/j.ijimpeng.2004.07.012.

Radford, D.D., Fleck, N.A., Deshpande, V.S., 2006a. The response of clamped sandwich beams subjected to shock loading. Int. J. Impact Eng. 32 (6), 968–987. http://dx.doi.org/10.1016/j.ijimpeng.2004.08.007.

Radford, D.D., McShane, G.J., Deshpande, V.S., Fleck, N.A., 2006b. The response of clamped sandwich plates with metallic foam cores to simulated blast loading. Int. J. Solids Struct. 43 (7–8), 2243–2259. http://dx.doi.org/10.1016/j.ijsolstr.2005.07.006.

Rathbun, H.J., Radford, D.D., Xue, Z., He, M.Y., Yang, J., Deshpande, V., Fleck, N.A., Hutchinson, J.W., Zok, F.W., Evans, A.G., 2006. Performance of metallic honeycomb-core sandwich beams under shock loading. Int. J. Solids Struct. 43 (6), 1746–1763. http://dx.doi.org/10.1016/j.ijsolstr.2005.06.079.

Rodriguez-Nikl, T., Hegemier, G., Seible, F., 2011. Blast simulator testing of structures: Methodology and validation. Shock Vib. 18 (4), 579–592. http://dx.doi.org/10.3233/SAV-2010-0563.

Schenk, M., Guest, S.D., McShane, G.J., 2014. Novel stacked folded cores for blast-resistant sandwich beams. Int. J. Solids Struct. 51 (25–26), 4196–4214. http://dx.doi.org/10.1016/j.ijsolstr.2014.07.027.

Shen, C., Yu, T., Lu, G., 2013. Double shock mode in graded cellular rod under impact. Int. J. Solids Struct. 50 (1), 217–233. http://dx.doi.org/10.1016/j.ijsolstr.2012.09.021.

Sun, Y.L., Li, Q.M., 2018. Dynamic compressive behaviour of cellular materials: A review of phenomenon, mechanism and modelling. Int. J. Impact Eng. 112, 74–115. http://dx.doi.org/10.1016/j.ijimpeng.2017.10.006.

Wadley, H.N., Børvik, T., Olovsson, L., Wetzel, J.J., Dharmasena, K.P., Hopperstad, O.S., Deshpande, V.S., Hutchinson, J.W., 2013. Deformation and fracture of impulsively loaded sandwich panels. J. Mech. Phys. Solids 61 (2), 674–699. http://dx.doi.org/10.1016/j.jmps.2012.07.007.

Wang, L.L., 2011. Foundations of Stress Waves. Elsevier.

Wang, E., Gardner, N., Shukla, A., 2009. The blast resistance of sandwich composites with stepwise graded cores. Int. J. Solids Struct. 46 (18–19), 3492–3502. http://dx.doi.org/10.1016/j.ijsolstr.2009.06.004.

Wang, Z., Jing, L., Ning, J., Zhao, L., 2011a. The structural response of clamped sandwich beams subjected to impact loading. Compos. Struct. 93 (4), 1300–1308. http://dx.doi.org/10.1016/j.compstruct.2010.05.011.

Wang, L.L., Yang, L.M., Ding, Y.Y., 2013a. On the energy conservation and critical velocities for the propagation of a steady-shock wave in a bar made of cellular material. Acta Mech. Sinica 29, 420–428. http://dx.doi.org/10.1007/s10409-013-0024-3.

Wang, X., Yu, R.P., Zhang, Q.C., Li, L., Li, X., Zhao, Z.Y., Han, B., He, S.Y., Lu, T.J., 2020. Dynamic response of clamped sandwich beams with fluid-fillied corrugated cores. Int. J. Impact Eng. 139, 103533. http://dx.doi.org/10.1016/j.ijimpeng.2020.103533.

Wang, Y., Zhao, W., Zhou, G., Wang, C., 2018a. Analysis and parametric optimization of a novel sandwich panel with double-v auxetic structure core under air blast loading. Int. J. Mech. Sci. 142–143, 245–254. http://dx.doi.org/10.1016/j.ijmecsci.2018.05.001.

Wang, X.K., Zheng, Z.J., Yu, J.L., 2013b. Crashworthiness design of density-graded cellular metals. Theor. Appl. Mech. Lett. 3 (3), 031001. http://dx.doi.org/10.1063/2.1303101.

Wang, X.K., Zheng, Z.J., Yu, J.L., Wang, C.F., 2011b. Impact resistance and energy absorption of functionally graded cellular structures. Appl. Mech. Mater. 69, 73–78. http://dx.doi.org/10.4028/www.scientific.net/AMM.69.73.

Wang, S.L., Zheng, Z.J., Zhu, C.F., Ding, Y.Y., Yu, J.L., 2018b. Crushing and densification of rapid prototyping polylactide foam: Meso-structural effect and a statistical constitutive model. Mech. Mater. 127, 65–76. http://dx.doi.org/10.1016/j.mechmat.2018.09.003.

Wei, X., Tran, P., De Vaucorbeil, A., Ramaswamy, R.B., Latourte, F., Espinosa, H.D., 2013. Three-dimensional numerical modeling of composite panels subjected to underwater blast. J. Mech. Phys. Solids 61 (6), 1319–1336. http://dx.doi.org/10.1016/j.jmps.2013.02.007.

Xiao, D., Chen, X., Li, Y., Wu, W., Fang, D., 2019. The structure response of sandwich beams with metallic auxetic honeycomb cores under localized impulsive loading-experiments and finite element analysis. Mater. Des. 176, 107840. http://dx.doi.org/10.1016/j.matdes.2019.107840.

Xiao, L., Song, W., Wang, C., Tang, H., Fan, Q., Liu, N., Wang, J., 2017. Mechanical properties of open-cell rhombic dodecahedron titanium alloy lattice structure manufactured using electron beam melting under dynamic loading. Int. J. Impact Eng. 100, 75–89. http://dx.doi.org/10.1016/j.ijimpeng.2016.10.006.

Yang, L.H., Qu, J., Yu, G.C., Yang, J.S., Wu, L.Z., 2018. The effect of strain-rate sensitivity on dynamic response of impulsively loaded sandwich beam. Mech. Adv. Mater. Struct. 26, 1743–1749. http://dx.doi.org/10.1080/15376494.2018.1447177.

Yang, J., Wang, S.L., Ding, Y.Y., Zheng, Z.J., Yu, J.L., 2017. Crashworthiness of graded cellular materials: A design strategy based on a nonlinear plastic shock model. Mater. Sci. Eng. A 680, 411–420. http://dx.doi.org/10.1016/j.msea.2016.11.010.

Yang, F., Xie, W., Meng, S., 2020. Impact and blast performance enhancement in bio-inspired helicoidal structures: A numerical study. J. Mech. Phys. Solids 142, 104025. http://dx.doi.org/10.1016/j.jmps.2020.104025.

Yu, T.X., Stronge, W.J., 1990. Large deflections of a rigid-plastic beam-on-foundation from impact. Int. J. Impact Eng. 9 (1), 115–126. http://dx.doi.org/10.1016/0734-743X(90)90025-Q.

Zhang, Y.R., Zhu, Y.D., Zheng, Z.J., Yu, J.L., 2022. A coupling analysis model of clamped monolithic beam impacted by foam projectile. Chin. J. Theor. Appl. Mech. 54, 2161–2172. http://dx.doi.org/10.6052/0459-1879-22-223 (in Chinese).

Zheng, Z.J., Liu, Y.D., Yu, J.L., Reid, S.R., 2012. Dynamic crushing of cellular materials: Continuum-based wave models for the transitional and shock modes. Int. J. Impact Eng. 42, 66–79. http://dx.doi.org/10.1016/j.ijimpeng.2011.09.009.

Zheng, Z.J., Wang, C.F., Yu, J.L., Reid, S.R., Harrigan, J.J., 2014. Dynamic stress–strain states for metal foams using a 3D cellular model. J. Mech. Phys. Solids 72, 93–114. http://dx.doi.org/10.1016/j.jmps.2014.07.013.